Molecular Cell

Resource

High-Resolution *In Vivo* Identification of miRNA Targets by Halo-Enhanced Ago2 Pull-Down

Graphical Abstract

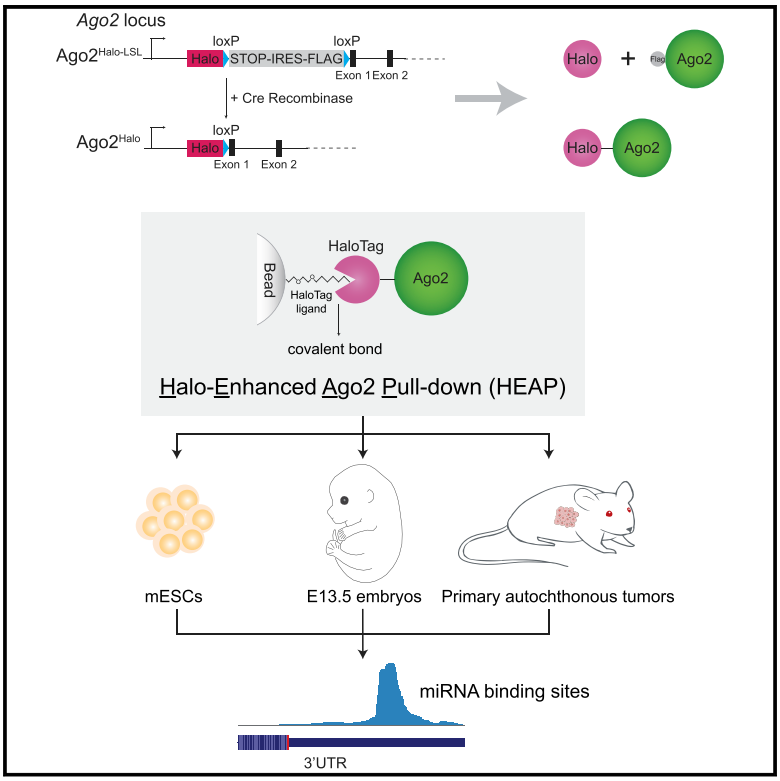

Highlights

- The authors describe a mouse strain harboring a Cre-regulated Halo-Ago2 knockin allele
- The model streamlines the experimental identification of miRNA-mRNA interactions
- The authors identify miRNA targets in mESCs, embryos, normal tissues, and tumors

Authors

Xiaoyi Li, Yuri Pritykin, Carla P. Concepcion, ..., Doron Betel, Christina S. Leslie, Andrea Ventura

Correspondence

cleslie@cbio.mskcc.org (C.S.L.), venturaa@mskcc.org (A.V.)

In Brief

Li, Pritykin, Concepcion et al. report the development of Halo-enhanced Ago2 pull-down (HEAP), a method that streamlines the experimental identification of Ago2-miRNA-mRNA interaction sites in murine cells and tissues.

Li et al., 2020, Molecular Cell 79, 167–179
July 2, 2020
https://doi.org/10.1016/j.molcel.2020.05.009

CellPress

Molecular Cell

CellPress

Resource

High-Resolution *In Vivo* Identification of miRNA Targets by Halo-Enhanced Ago2 Pull-Down

Xiaoyi Li,[1,2,17] Yuri Pritykin,[3,17] Carla P. Concepcion,[2,4,5,17] Yuheng Lu,[3,6] Gaspare La Rocca,[2] Minsi Zhang,[2,7] Bryan King,[2] Peter J. Cook,[2,8] Yu Wah Au,[2,9] Olesja Popow,[10,11,12] Joao A. Paulo,[12] Hannah G. Otis,[3,13] Chiara Mastroleo,[2] Paul Ogrodowski,[2] Ryan Schreiner,[14] Kevin M. Haigis,[10,11,12] Doron Betel,[15,16] Christina S. Leslie,[3,*] and Andrea Ventura[2,18,*]

[1]Louis V. Gerstner Jr. Graduate School of Biomedical Sciences, Memorial Sloan Kettering Cancer Center, New York, NY 10065, USA
[2]Cancer Biology and Genetics Program, Memorial Sloan Kettering Cancer Center, New York, NY 10065, USA
[3]Computational and Systems Biology Program, Memorial Sloan Kettering Cancer Center, New York, NY 10065, USA
[4]Weill Cornell Graduate School of Medical Sciences, Cornell University, New York, NY 10065, USA
[5]Koch Institute for Integrative Cancer Research, Massachusetts Institute of Technology, Cambridge, MA 02139, USA
[6]Department of Systems Biology, Harvard Medical School, Boston, MA 02115, USA
[7]Department of Radiation Oncology, Memorial Sloan Kettering Cancer Center, New York, NY 10065, USA
[8]Center for Immunity and Immunotherapies, Seattle Children's Research Institute, Seattle, WA 98101, USA
[9]Department of Internal Medicine (Nephrology), Leiden University Medical Center, Zuid-Holland, 2333 ZA, the Netherlands
[10]Department of Cancer Biology, Dana-Farber Cancer Institute, Boston, MA 02215, USA
[11]Department of Medicine, Brigham & Women's Hospital and Harvard Medical School, Boston, MA 02115, USA
[12]Department of Cell Biology, Harvard Medical School, Boston, MA 02115, USA
[13]Weill Cornell/Rockefeller/Sloan Kettering Tri-Institutional MD-PhD Program, New York, NY 10065, USA
[14]Margaret Dyson Vision Research Institute, Department of Ophthalmology, Weill Cornell Medical College, New York, NY 10065, USA
[15]Division of Hematology and Medical Oncology, Department of Medicine, Weill Cornell Medical College, New York, NY 10065, USA
[16]Institute for Computational Biomedicine, Weill Cornell Medical College, New York, NY 10065, USA
[17]These authors contributed equally
[18]Lead Contact
*Correspondence: cleslie@cbio.mskcc.org (C.S.L.), venturaa@mskcc.org (A.V.)
https://doi.org/10.1016/j.molcel.2020.05.009

SUMMARY

The identification of microRNA (miRNA) targets by Ago2 crosslinking-immunoprecipitation (CLIP) methods has provided major insights into the biology of this important class of non-coding RNAs. However, these methods are technically challenging and not easily applicable to an *in vivo* setting. To overcome these limitations and facilitate the investigation of miRNA functions *in vivo*, we have developed a method based on a genetically engineered mouse harboring a conditional Halo-Ago2 allele expressed from the endogenous Ago2 locus. By using a resin conjugated to the HaloTag ligand, Ago2-miRNA-mRNA complexes can be purified from cells and tissues expressing the endogenous Halo-Ago2 allele. We demonstrate the reproducibility and sensitivity of this method in mouse embryonic stem cells, developing embryos, adult tissues, and autochthonous mouse models of human brain and lung cancers. This method and the datasets we have generated will facilitate the characterization of miRNA-mRNA networks *in vivo* under physiological and pathological conditions.

INTRODUCTION

A key challenge in deciphering the biological functions of microRNAs (miRNAs) remains the identification of their targets *in vivo* under physiological and pathological conditions. Although significant progress has been made in computational methods to predict miRNA binding sites (Agarwal et al., 2015; Bartel, 2009; Friedman et al., 2009; Grimson et al., 2007), these methods do not take into account several known and unknown variables that determine whether a "potential" target site is in fact available and bound by a miRNA in a given cellular context. To complement computational approaches, biochemical methods to purify Ago2-miRNA-mRNA complexes have been developed (Chi et al., 2009; Grosswendt et al., 2014; Hafner et al., 2010; Helwak et al., 2013; König et al., 2010; Moore et al., 2015; Van Nostrand et al., 2016). Although the details vary, these methods rely on the use of antibodies to precipitate Argonaute-containing complexes, usually after UV crosslinking, followed by high-throughput sequencing of the associated mRNAs.

While these methods have been applied with substantial success to map miRNA-mRNA interactions in cell lines, they are used much less extensively *in vivo* due to their technical

complexity and the lack of efficient ways to restrict the analysis to specific cell types within a tissue. To overcome these limitations, we have developed a method, Halo-enhanced Ago2 pull-down (HEAP), which utilizes a tagged version of the Ago2 protein and allows the direct purification of Ago2-containing complexes bypassing the need for radiolabeling, immunoprecipitation, and gel purification. To facilitate the application of this method *in vivo*, we have generated a mouse strain in which a conditional allele of Halo-tagged Ago2 is knocked into the endogenous *Ago2* locus and activated upon exposure to Cre recombinase.

To benchmark the HEAP method, we applied it to identify miRNA targets in diverse cellular contexts, including murine embryonic stem cells (mESCs), wild-type and miR-17∼92 null mid-gestation mouse embryos, adult mouse lungs, adult mouse brains, and three distinct autochthonous mouse models of human lung and brain cancers. As a result, we have identified a large number of miRNA targets at high resolution and demonstrated the reproducibility and sensitivity of the HEAP method.

The datasets and the tools generated in this study reveal the complex landscape of miRNA targeting *in vivo* and will facilitate future studies aimed at characterizing the biological functions of this important class of small non-coding RNAs under physiological and pathological conditions.

RESULTS

A Halo-Ago2 Fusion Protein Enables Antibody-free Purification of miRNA Targets

The HaloTag is a 33-kDa haloalkane dehalogenase encoded by the *DhaA* gene from *Rhodococcus rhodochrous* that has been mutagenized to form an irreversible covalent bond to synthetic chloroalkane ligands (collectively known as HaloTag ligands) (Encell et al., 2012; Los et al., 2008). Linking the chloroalkane ligand to a solid substrate enables the efficient purification of fusion proteins containing the HaloTag (Figure 1A). Importantly, Gu and colleagues have recently used the HaloTag together with UV crosslinking to efficiently identify RNA targets of the RNA binding protein PTB (Gu et al., 2018).

To determine whether a similar strategy can be employed to purify complexes containing Ago2 proteins bound to miRNA and target mRNAs, we fused the HaloTag to the N terminus of Ago2 (Halo-Ago2; Figure 1A). When expressed in $Ago2^{-/-}$ mouse embryonic fibroblasts (MEFs) (O'Carroll et al., 2007), the Halo-Ago2 fusion protein localized largely to the cytoplasm, while the HaloTag alone displayed uniform localization to both the cytoplasm and the nucleus (Figure 1B; Data S1). Importantly, the Halo-Ago2 construct was nearly as effective as wild-type Ago2 at rescuing RNAi in $Ago2^{-/-}$ MEFs, indicating that the Halo-Ago2 fusion protein retains slicing activity (Figure 1C).

To avoid artifacts due to ectopic expression of Halo-Ago2 and enable the isolation of Ago2 complexes directly from murine tissues, we knocked in the HaloTag cassette into the endogenous *Ago2* locus in mESCs (Figure 1D). In this knockin allele, the HaloTag is separated from the first coding exon of *Ago2* by an in-frame *loxP*-STOP-IRES-FLAG-*loxP* (LSL) cassette ($Ago2^{Halo\text{-}LSL}$). Cells harboring this allele express a bicistronic mRNA encoding for two proteins, the HaloTag and a Flag-Ago2 fusion protein whose translation is initiated by an internal ribosomal entry site (IRES). Upon expression of the Cre recombinase, the LSL cassette is excised and the HaloTag is now brought in frame with the first coding exon of *Ago2*, thus resulting in expression of the Halo-Ago2 fusion protein (Figures 1D and 1E). The recombined allele expressing the Halo-Ago2 fusion will be hereafter referred to as $Ago2^{Halo}$.

We first tested whether the $Ago2^{Halo}$ allele could be used to map miRNA-mRNA interactions in mESCs. For these experiments, we adapted the Ago2 high-throughput sequencing of RNA isolated by crosslinking immunoprecipitation (Ago2 HITS-CLIP) method originally developed by the Darnell group (Chi et al., 2009) with two significant streamlining modifications enabled by the covalent bond between Halo-Ago2 and the HaloTag ligand. First, instead of using anti-Ago2 antibodies to isolate Ago2-containing complexes, we used Sepharose beads covalently linked to the HaloTag ligand. Second, the radiolabeling and SDS-PAGE purification step necessary in CLIP protocols to purify RNAs bound to Ago2 were omitted and replaced by extensive washes followed by direct RNA extraction from beads, library construction, and high-throughput sequencing of Halo-Ago2-bound miRNAs and mRNAs. We refer to this method as HEAP (Figure 1F). By performing HEAP, two types of libraries are generated: a target library (mRNAs) and a miRNA library (Figures 1F and S1A). The former allows the identification of miRNA binding sites on their targets, while the latter provides an estimate of miRNA abundance.

When mapped to the mouse genome, HEAP mRNA libraries generated from $Ago2^{Halo/+}$ mESCs, but not those generated from control $Ago2^{Halo\text{-}LSL/+}$ cells, produced well-defined "clusters" of reads, hereafter referred to as "peaks" (Figures S1A and S1B). To facilitate the identification of these peaks, we adapted the "SMInput" protocol used in enhanced-CLIP (eCLIP) (Van Nostrand et al., 2016) and generated input control libraries from size-matched RNA fragments isolated after the limited RNase protection step (Figure 1F). We first identified putative peaks using the CLIPanalyze package (https://bitbucket.org/leslielab/clipanalyze), an improved peak-calling algorithm based on edge detection technique similar to methods from image processing (Hsin et al., 2018; Lianoglou et al., 2013; Loeb et al., 2012). CLIPanalyze uses the input control libraries as background to assign a p value to each peak, performing library size normalization based on reads aligned across the genome outside of putative peaks (see also STAR Methods for additional details).

To determine the sensitivity and reproducibility of the HEAP method, we generated HEAP libraries from three $Ago2^{Halo/+}$ mESC clones (using 1.5×10^8 cells per library). By combining the three libraries, CLIPanalyze identified a total of 30,564 putative Ago2 binding sites at an adjusted p value cutoff of 0.05. Previous studies have demonstrated that 3′ untranslated regions (3′ UTRs) of mRNAs are the preferred, although not exclusive, sites of interaction between miRNAs and mRNAs (Bartel, 2018; Chi et al., 2009; Sarshad et al., 2018). Consistent with these findings, the majority of HEAP peaks we identified in mESCs mapped to 3′ UTRs, followed by sites mapping to protein coding sequences (CDS) (Figures 2A and S1C). The fractions of 3′ UTR and CDS peaks increased monotonically with their statistical significance, while intergenic and intronic peaks had the opposite behavior. For example, when examining the 1,000 most statistically significant peaks, greater than

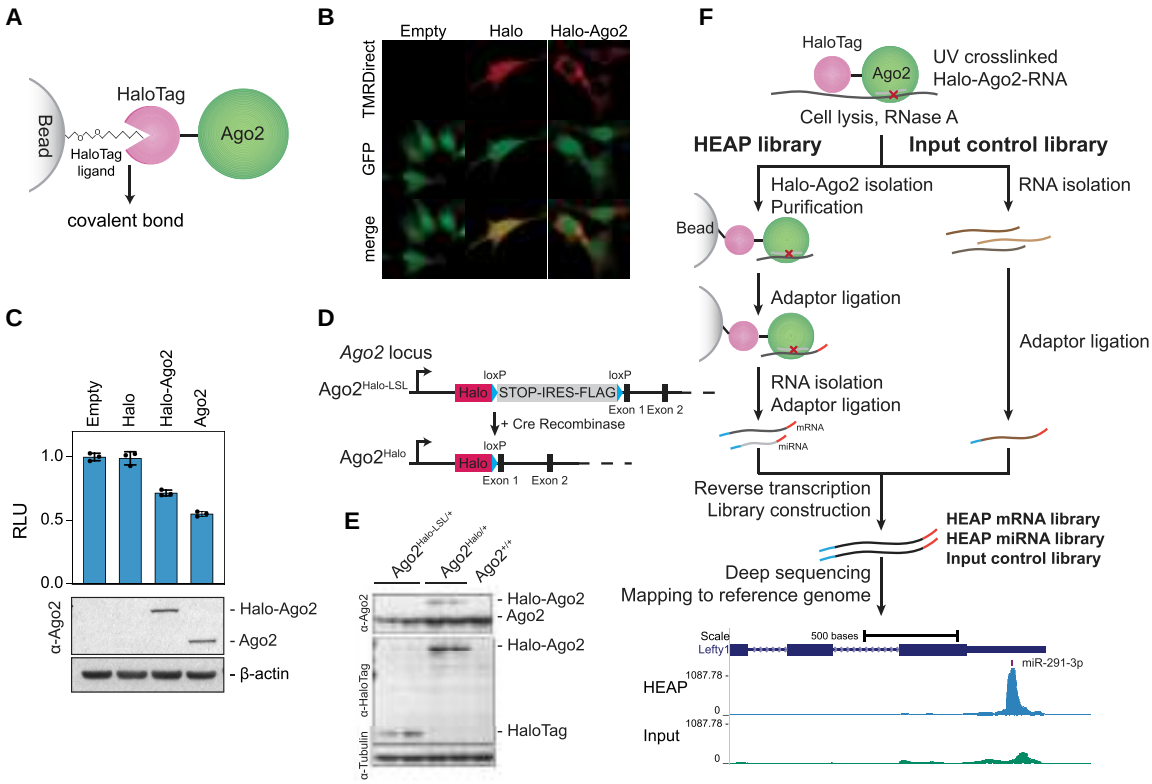

Figure 1. Halo-Enhanced Ago2 Pull-Down (HEAP)

(A) Schematic of the Halo-Ago2 fusion protein covalently bound to a bead-conjugated HaloTag ligand.

(B) *Ago2*$^{-/-}$ immortalized MEFs transduced with MSCV-PIG, MSCV-PIG-Halo, or MSCV-PIG-Halo-Ago2 retroviruses were incubated with the HaloTag TMRDirect ligand and imaged. Notice the prevalently cytoplasmic localization of the Halo-Ago2 fusion protein.

(C) *Ago2*$^{-/-}$ MEFs transduced with retroviral vectors encoding HaloTag alone, full-length Ago2, or the Halo-Ago2 fusion protein were transiently transfected with reporter plasmids expressing Firefly and Renilla luciferase and a plasmid expressing a short hairpin RNA (shRNA) against the Firefly luciferase. The ratio between Firefly and Renilla luciferase activity was measured 48 h after transfection (upper panel). Whole-cell lysates from the same cells were probed with antibodies against Ago2 and β-actin (lower panel). Error bars represent mean ± SD.

(D) Schematic of the targeting strategy used to generate the Halo-Ago2 conditional knockin allele. Halo, HaloTag; STOP, stop codon; IRES, internal ribosome entry site.

(E) Whole-cell lysates from mESCs with the indicated genotypes were probed with antibodies against Ago2, HaloTag, and tubulin.

(F) Outline of the strategy used to generate HEAP and input control libraries (upper panel) and a representative Halo-Ago2 binding site identified in mESCs (lower panel).

See also Figures S1A and S1B and Data S1.

50% of them mapped to 3′ UTRs and less than 3% mapped to introns (Figure 2A). To measure reproducibility, we applied the CLIPanalyze algorithm independently to each library and performed pairwise irreproducible discovery rate (IDR) (Li et al., 2011) analysis. On average, this analysis identified 80% of peaks as reproducible at IDR < 0.05, demonstrating the robustness of the HEAP method (Figure S1D). We also generated a series of HEAP libraries using decreasing numbers of mESCs (from 1.5×10^8 to 1×10^3). As expected, the total number of confidently identified peaks progressively decreased as the amount of starting material was reduced (Figure S1E). The most robust peaks could be identified in libraries generated from as few as 5×10^5 mESCs (Figure S1F), but for optimal results, we recommend starting from a minimum of 1×10^7 mESCs. Since mESCs have little cytoplasm, the detection limit is likely to be lower for cell types with more abundant cytoplasm.

To gain additional insights into the nature of peaks identified by HEAP, we searched for enriched 7-mers in the sequences underlying peaks mapping to 3′ UTRs (Figure S1G). Inspection of the resulting motifs revealed a marked enrichment for seed matches corresponding to miRNA families whose members are collectively highly expressed in mESCs (Figures 2B and S1H). We also observed a positive correlation between the relative abundance of individual miRNA families (estimated from the miRNA libraries) and the number of corresponding peaks identified by HEAP (Figure 2C).

To directly test whether the peaks identified by HEAP reflect true miRNA-mRNA interactions, we selected a robust peak identified in the 3′ UTR of the *Lefty2* mRNA (Figure 2D). The sequence underlying this peak includes a highly conserved 8-mer that is complementary to the miR-291-3p seed (Figure S1I). We used CRISPR-Cas9 and homologous recombination in mESCs to introduce point

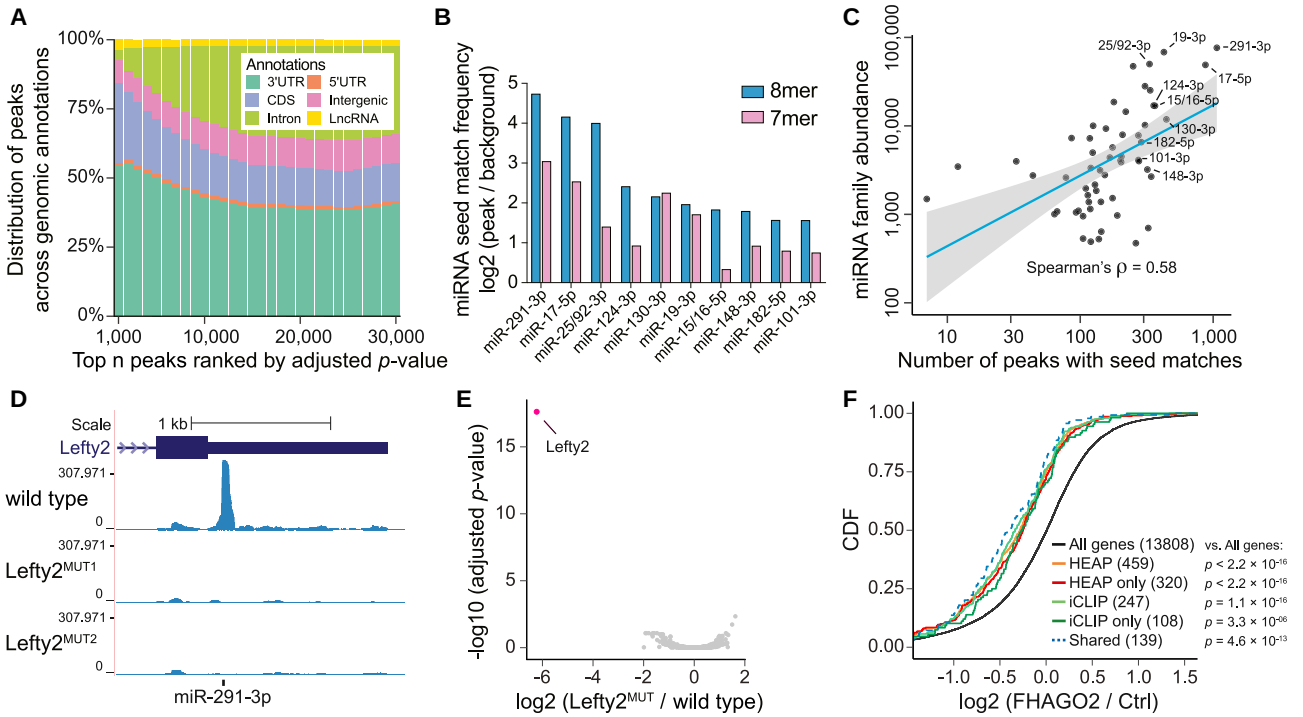

Figure 2. Mapping Halo-Ago2 Binding Sites in mESCs

(A) Peaks identified in the HEAP libraries from mESCs were ranked by increasing adjusted p value before calculating their distribution across genomic annotations. CDS, coding sequence; 5′ UTR, 5′ untranslated region; 3′ UTR, 3′ untranslated region; LncRNA, long non-coding RNA.

(B) Enrichment for sequences complementary to murine miRNA seeds (7-mers and 8-mers) was calculated comparing 3′ UTR sequences within and outside HEAP peaks. The bar plot shows enrichment for the top 10 miRNA seed families ranked by 8-mer enrichment scores.

(C) Scatterplot showing the correlation between number of 3′ UTR peaks with 7-mer or 8-mer seed matches to individual miRNA families and abundance of their corresponding miRNAs as measured in HEAP miRNA libraries. Blue line represents best-fit linear regression, with 95% confidence interval in gray.

(D) Genome browser view of the *Lefty2* 3′ UTR with tracks corresponding to libraries generated from wild-type mESCs or cells harboring targeted mutations disrupting the predicted miR-291-3p binding site (*Lefty2*^{MUT1} and *Lefty2*^{MUT2}).

(E) Volcano plot of global changes in HEAP peak intensity between the *Lefty2*^{MUT} and wild-type mESC libraries. Notice the selective loss of the *Lefty2* 3′ UTR binding site (highlighted).

(F) Cumulative distribution function (CDF) plot for targets of miR-291-3p identified by iCLIP or HEAP. The log2-fold change was calculated in *Ago1-4*$^{-/-}$ mESCs upon ectopic FHAGO2 expression. HEAP only, targets identified uniquely by HEAP; iCLIP only, targets identified uniquely by iCLIP; shared, targets identified by both methods. p value, two-sided Kolmogorov-Smirnov test.

See also Figures S1C–S1I and S2. See Data S2 for peaks identified in mESCs.

mutations designed to disrupt this seed match (Figure S1I). HEAP libraries generated from two independent *Lefty2*^{MUT} clones showed complete and selective loss of the Lefty2 peak, further demonstrating the ability of the HEAP method to map bona fide miRNA-mRNA interactions in cells (Figures 2D and 2E).

To assess the ability of HEAP to identify functional miRNA binding sites, we analyzed an RNA sequencing (RNA-seq) dataset generated by Bosson and colleagues from mESCs null for all four Argonaute proteins (*Ago1-4*$^{-/-}$) in the presence or absence of exogenously expressed FLAG- and hemagglutinin (HA)-tagged AGO2 (FHAGO2; Bosson et al., 2014; GEO: GSE61348). Introduction of FHAGO2 in *Ago1-4*$^{-/-}$ cells should restore miRNA function, causing repression of their targets. In agreement with this prediction, miRNA targets identified by HEAP were preferentially repressed upon FHAGO2 reintroduction (Figure S2A). The effect was particularly strong for targets assigned by HEAP to the most abundantly expressed miRNA families in mESCs. For example, we observed the strongest repression for targets of the miR-291-3p, miR-17-5p and miR-148-3p families, three miRNA families that account for greater than 12% of all miRNAs in mESCs (Figure S2A; data not shown). Peaks with lower adjusted p values or higher log2-fold changes (HEAP versus input control) were associated with stronger target repression (Figure S2B). As expected, peaks mapping to 3′ UTRs were associated with strongest target repression compared to peaks mapping to other genomic annotations (Figure S2C).

This analysis also allowed us to compare miRNA targets identified by HEAP to those previously identified by Bosson et al. in Ago1-4$^{-/-}$-FHAGO2 mESCs using individual-nucleotide resolution crosslinking and immunoprecipitation (iCLIP), a well-established variant of HITS-CLIP (König et al., 2010). By applying the CLIPanalyze peak calling algorithm, we identified 6,813 miRNA binding sites in their iCLIP library and nearly twice as many (on average 13,532) in each of the three HEAP mESC libraries. The iCLIP library also identified fewer peaks mapping to 3′ UTR

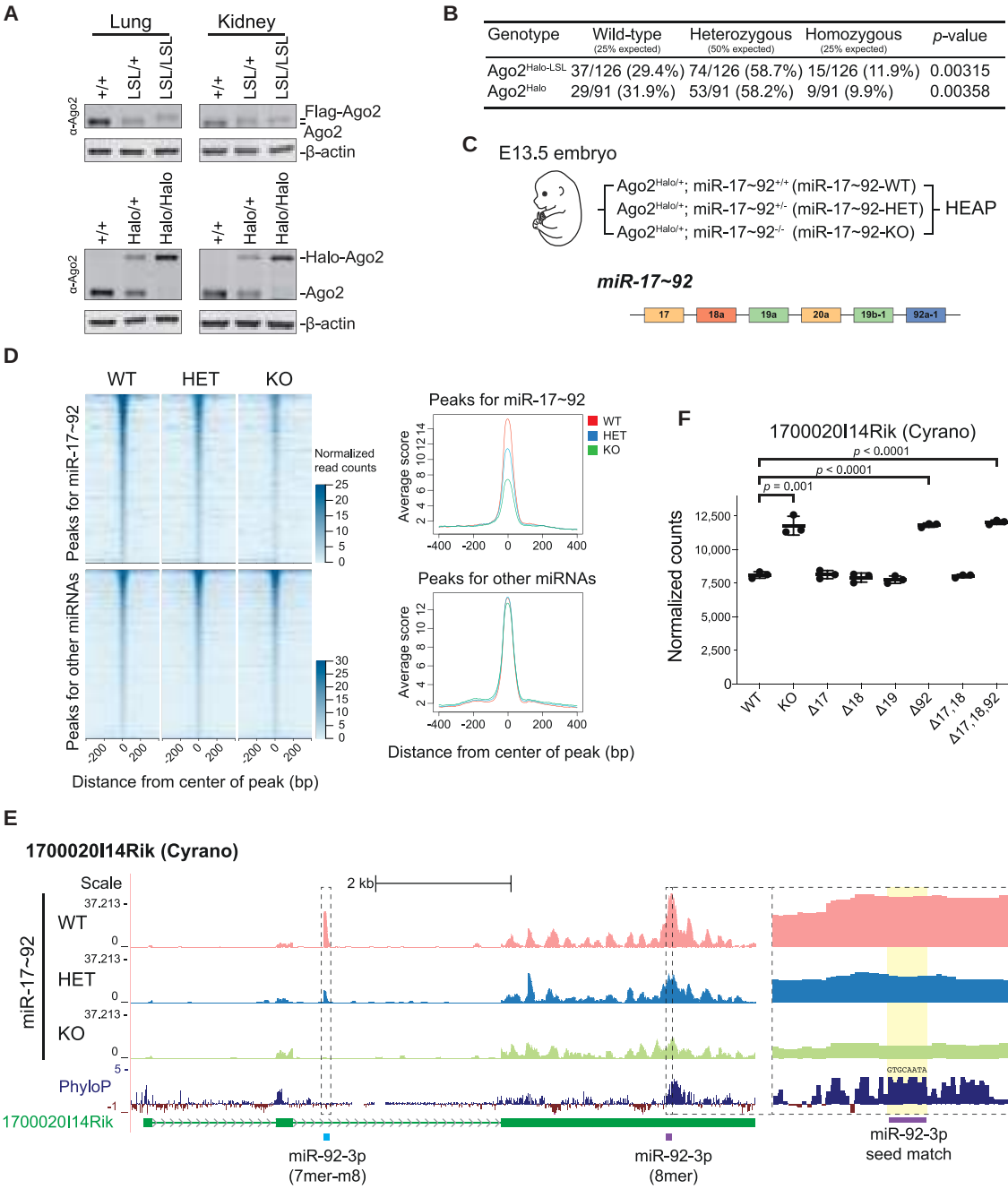

Genotype	Wild-type (25% expected)	Heterozygous (50% expected)	Homozygous (25% expected)	*p*-value
$Ago2^{Halo\text{-}LSL}$	37/126 (29.4%)	74/126 (58.7%)	15/126 (11.9%)	0.00315
$Ago2^{Halo}$	29/91 (31.9%)	53/91 (58.2%)	9/91 (9.9%)	0.00358

Figure 3. Identification of miR-17~92 Targets in E13.5 Embryos

(A) Expression of Ago2 fusion proteins in the lungs and kidneys of *Ago2*$^{Halo\text{-}LSL}$ and *Ago2*^{Halo} mice. +/+, wild type; LSL, *Ago2*$^{Halo\text{-}LSL}$; Halo: *Ago2*^{Halo}.

(B) Absolute numbers and frequencies of genotypes obtained from heterozygous intercrosses of *Ago2*$^{Halo\text{-}LSL/+}$ or *Ago2*$^{Halo/+}$ mice. p value, chi-square test.

(C) Outline of the HEAP experiments in E13.5 *Ago2*$^{Halo/+}$ embryos wild-type, heterozygous, or homozygous knockout for the miR-17~92 cluster. A schematic of the miR-17~92 cluster is shown at the bottom. miRNA members are color-coded based on their seed sequences.

(D) Heatmap and histogram of peak signal in an 800-bp region surrounding HEAP peaks obtained from miR-17~92-WT, miR-17~92-HET, and miR-17~92-KO E13.5 embryos. Peaks containing seed matches for the top 31 miRNA seed families ranked by abundance were chosen. Peaks with seed matches for miRNAs belonging to the miR-17~92 cluster are plotted in the upper panels, while the remaining peaks are plotted in the lower panels.

(E) Genome browser view of the miR-92a-1-dependent miRNA binding sites detected in the long non-coding RNA *1700020I14Rik (Cyrano)*. PhyloP: placental mammal basewise conservation by PhyloP. Notice the highly conserved 8-mer seed match for miR-92-3p under the second peak.

(legend continued on next page)

and more peaks mapping to intergenic regions compared to the HEAP libraries (Figure S2D).

3′ UTR targets for miR-291-3p seed family identified by both methods were associated with strong repression of the corresponding genes upon FHAGO2 reintroduction (Figure 2F). The overlap between miR-291-3p binding sites identified by iCLIP and HEAP in 3′ UTRs was partial, with the HEAP target pool being nearly twice as large (Figure S2E). Importantly, the targets identified only by HEAP also displayed strong repression upon FHAGO2 reintroduction, indicating that they are functional miRNA binding sites (Figure 2F). We further confirmed the ability of HEAP to identify functional miRNA targets by measuring mRNA and protein expression changes of HEAP targets upon inactivation of Dicer1, the key enzyme responsible for miRNA maturation, in mESCs (Figure S2F).

Collectively, these results show that HEAP provides an effective method to identify miRNA-mRNA interactions in cells.

A Conditional Halo-Ago2 Mouse Enables Identification of miRNA-mRNA Interactions *In Vivo*

The accurate identification of miRNA targets *in vivo* and in a cell-type-specific context is essential to dissect the functions of miRNAs in development, homeostasis, and disease. To translate the HEAP method to an *in vivo* setting, we used mESCs harboring the Cre-inducible Halo-Ago2 allele to generate *Ago2*$^{Halo\text{-}LSL/+}$ mice. We then crossed these animals to *CAG-Cre* mice (Sakai and Miyazaki, 1997) to delete the LSL cassette and induce ubiquitous expression of the endogenous Halo-Ago2 allele. PCR in MEFs and immunoblot analysis in MEFs and tissues derived from these mice confirmed efficient deletion of the LSL cassette and expression of the Halo-Ago2 protein (Figures 3A, S3A, and S3B). Although *Ago2*-$^{Halo/+}$ and *Ago2*$^{Halo\text{-}LSL/+}$ mice were obtained at the expected Mendelian frequency and phenotypically indistinguishable from wild-type mice, homozygous mice for the *Ago2*^{Halo} or the *Ago2*$^{Halo\text{-}LSL}$ alleles were recovered at sub-Mendelian frequencies (9.9% and 11.9%, respectively, compared to the expected 25%; Figure 3B). The sub-Mendelian recovery of homozygous mice might reflect lower Ago2 expression levels compared to wild-type mice (Figures 3A and S3B) and/or an impaired miRNA-induced silencing complex (miRISC) formation or activity caused by the presence of the N-terminal tag. Size-exclusion chromatography in *Ago2*$^{Halo/+}$ cells showed the Halo-Ago2 fusion protein co-eluting with wild-type Ago2 in high-molecular-weight complexes (Figure S3C), and pull-down experiments confirmed the physical interaction between Halo-Ago2 and Tnrc6a, a core component of the miRISC (Figure S3D). Furthermore, reporter experiments using multiple luciferase reporter constructs harboring well-characterized miRNA binding sites, as well as a highly sensitive two-color fluorescent reporter system (Mukherji et al., 2011), showed no detectable differences in miRNA-mediated repression between wild-type and *Ago2*$^{Halo/Halo}$ MEFs (Figures S3E and S3F). A careful comparison of RNA-seq libraries generated from wild-type and *Ago2*$^{Halo/Halo}$ cells, however, revealed a slight preferential de-repression of targets of the most highly expressed miRNA families (Figure S3G). Due to the importance of miRNA-mediated gene regulation during embryonic development, it is possible that this modest perturbation of miRISC activity is responsible for the observed reduced viability of homozygous mice.

To test whether endogenously expressed Halo-Ago2 can be used to identify miRNA targets *in vivo*, we crossed *Ago2*$^{Halo/+}$ mice to mice harboring a targeted deletion of the miR-17∼92 locus (*Mirc1*), a polycistronic miRNA cluster encoding six distinct miRNAs, which has been shown to be essential for mammalian development (Han et al., 2015; Ventura et al., 2008). We generated HEAP libraries from *Ago2*$^{Halo/+}$*; miR-17∼92*$^{+/+}$ (miR-17∼92-WT), *Ago2*$^{Halo/+}$*; miR-17∼92*$^{+/-}$ (miR-17∼92-HET) and *Ago2*$^{Halo/+}$*; miR-17∼92*$^{-/-}$ (miR-17∼92-KO) embryonic day 13.5 (E13.5) embryos (Figure 3C). At an adjusted p value cutoff of 0.01, HEAP identified a total of 8,661 peaks in these libraries, with a distribution across genomic annotations similar to that observed in mESCs (Figure S4A). Importantly, the intensity of peaks containing seed matches to members of the miR-17∼92 cluster was markedly reduced—in a dose-dependent fashion—in the libraries generated from miR-17∼92-HET and miR-17∼92-KO embryos (Figure 3D). The murine genome contains two additional miRNA clusters that are paralogs to miR-17∼92 and encode similar miRNAs (Ventura et al., 2008), which may explain some residual Halo-Ago2 binding to these sites even in the homozygous mutants. Using an RNA-seq dataset previously generated in the lab from E9.5 embryos harboring an allelic series of miR-17∼92 mutant alleles (Han et al., 2015; GEO: GSE63813), we demonstrated that HEAP targets containing seed matches for miR-17/20-5p, miR-19-3p, and miR-92-3p mediated strong target repression (Figure S4B). The effect was particularly evident when considering genes harboring HEAP peaks for miR-17/20-5p and miR-92-3p, whose signal intensities were reduced in the miR-17∼92-KO embryo, confirming the importance of combining biochemical and genetic approaches to study miRNA function.

Interestingly, we also identified a sizeable fraction of reproducible peaks (4%) mapping to non-coding RNAs. These included two previously uncharacterized miR-17∼92-dependent sites matching the miR-92-3p seed in the long non-coding RNA *Cyrano* (Kleaveland et al., 2018; Ulitsky et al., 2011) (Figure 3E). Importantly, we observed significant upregulation of *Cyrano* in mouse E9.5 embryos lacking miR-92a-1, but not in mice harboring selective deletion of the other members of the cluster (Figure 3F) (Han et al., 2015), suggesting these binding sites are functional. These results demonstrate the usefulness of the Halo-Ago2 mouse strain in facilitating the identification of miRNA targets *in vivo*.

(F) RNA expression of *Cyrano* in the heart of E9.5 embryos harboring an allelic series of miR-17∼92 mutant alleles. KO, embryos null for the entire miR-17∼92 cluster; Δ17, embryos null for miR-17 and miR-20a; Δ18, embryos null for miR-18a; Δ19, embryos null for miR-19a and miR-19b-1, Δ92, embryos null for miR-92a-1; Δ17,18, embryos null for miR-17, miR-18a, and miR-20a; Δ17,18,92, embryos null for miR-17, miR-18a, miR-20a, and miR-92a-1. Notice that *Cyrano* is only upregulated in mutants in which miR-92a-1 is deleted. p value, unpaired t test. Data are represented as mean ± SD.
See also Figures S3 and S4. See Data S2 for peaks identified in E13.5 embryos.

To directly compare the performance of HEAP to immunoprecipitation-based approaches *in vivo*, we next generated libraries from the cortex of P13 *Ago2*$^{Halo/+}$ mice, a tissue from which high-quality miRNA target libraries have been previously generated by HITS-CLIP and CLEAR (covalent ligation of endogenous Argonaute-bound RNAs)-CLIP (Chi et al., 2009; Moore et al., 2015). Two HEAP libraries generated from the cortices of *Ago*$^{Halo/+}$ mice produced 7,069 peaks at an adjusted p value cutoff of 0.05. This number of miRNA-mRNA interaction sites is comparable to that identified by Moore and colleagues (CLEAR-CLIP, GEO: GSE73059, n = 7,927) using 12 biological replicates (Figures S4C and S4D). HEAP and CLEAR-CLIP identified similar numbers of targets for miR-124-3p, one of the most abundant miRNA families in the mouse cortex (Figure S4E). When benchmarked against a microarray gene expression dataset generated from neuroblastoma cells (CAD) ectopically expressing miR-124 (Makeyev et al., 2007; GEO: GSE8498), HEAP and CLEAR-CLIP were equally effective at identifying miR-124 target sites that mediated target repression (Figure S4F). Collectively, these results demonstrate that the HEAP method provides a simple and cost-effective approach to identify miRNA-mRNA interactions during murine development and in primary tissues.

Identification of miRNA Targets in Normal Adult Tissues and Autochthonous Tumors

We next tested whether the conditional Halo-Ago2 mouse could be used to identify miRNA-mRNA interactions in primary autochthonous tumors and in their tissues of origin. We first chose a mouse model of glioma driven by the *Bcan-Ntrk1* gene fusion that we recently developed in our laboratory (Cook et al., 2017). In this model, *Trp53*$^{fl/fl}$ mice are injected intracranially with a mixture of two recombinant adenoviruses. The first (Ad-BN) expresses Cas9 and two single-guide RNAs (sgRNAs) designed to induce the *Bcan-Ntrk1* rearrangement, an intrachromosomal deletion resulting in the fusion between the N-terminal portion of Bcan and the kinase domain of Ntrk1. The second adenovirus expresses the Cre recombinase (Ad-Cre) to achieve concomitant deletion of *Trp53* and allow glioma formation. By performing this procedure in ~4- to 6-week-old *Ago2*$^{Halo\text{-}LSL/+}$; *Trp53*$^{fl/fl}$ mice, we produced Bcan-Ntrk1-driven gliomas expressing the endogenous Halo-Ago2 allele.

We generated HEAP libraries from three independent Bcan-Ntrk1 gliomas and the normal cortices of three age-matched *Ago2*$^{Halo/+}$ mice. Quantification of miRNA abundance in HEAP miRNA libraries revealed drastic differences between the two tissues, with 77 miRNA seed families (26 broadly conserved) being significantly upregulated in gliomas and 77 families (18 broadly conserved) downregulated (adjusted p value < 0.05, absolute log2FC > 0.5; Figure 4A). Of note, the significantly downregulated families include miR-124-3p and miR-128-3p, two miRNA families that are highly expressed in the cortex of mice (Bak et al., 2008; Landgraf et al., 2007) and functionally important in the mouse central nervous system as suggested by genetic loss-of-function studies (Sanuki et al., 2011; Tan et al., 2013). Additionally, members of the oncogenic miRNA cluster miR-17~92 (He et al., 2005; Ota et al., 2004) were among the most strongly upregulated miRNAs in gliomas, suggesting the possibility that these miRNAs are functionally relevant in gliomagenesis.

Using an adjusted p value cutoff of 0.05, we identified 1,878 Halo-Ago2 binding sites in tumors and 2,688 sites in normal cortices, with an overlap of 1,335 sites. Peak distribution across genomic annotations was similar between the two tissues, with the majority of peaks mapping to 3′ UTRs (Figure 4B). Analysis of seed matches under the peaks revealed marked differences between normal and neoplastic brains. Motifs complementary to the seeds of miR-219a-5p, miR-17-5p, miR-15/16-5p, miR-181-5p, and miR-130-3p were preferentially enriched in peaks identified in gliomas, while motifs complementary to the seeds of miR-124-3p, miR-29-3p, miR-9-5p, miR-128-3p, miR-137-3p, miR-138-5p, and miR-7-5p were preferentially enriched in peaks from normal cortices (Figures 4C, 4F, and S5A). Targets for the let-7-5p family of miRNAs were also abundant, but not differentially represented between the normal brain and tumors (Figures 4C and S5A). The enrichment for specific seed matches observed in the two conditions reflected in large part the differential expression of the corresponding miRNAs (Figure 4D) and resulted in differential gene regulation, as demonstrated by a statistically significant repression of miR-219a-5p targets in gliomas and of miR-124-3p targets in the normal cortices (Figure 4E).

Among all miRNA families, the miR-219a-5p family had the highest number of targets in gliomas (300 out of 1,878 peaks containing 6-mer, 7-mer, or 8-mer seed matches to miR-219a-5p). miR-219a-5p has been reported to regulate oligodendrocyte differentiation and myelination in mice via targeting important regulators of oligodendrocyte progenitor cell (OPC) maintenance (Dugas et al., 2010; Emery, 2010; Fan et al., 2017; Wang et al., 2017; Zhao et al., 2010). Interestingly, we observed a strong interaction between miR-219a-5p and *Pdgfra* (Figure 4F), a characteristic marker of OPCs and a key player in gliomagenesis.

Finally, to extend the application of the HEAP method to other tumor types, we mapped miRNA-mRNA interactions in two murine models of non-small cell lung cancer (NSCLC), the Cre recombinase-mediated *KRas*$^{LSL\text{-}G12D/+}$; *Trp53*$^{fl/fl}$ (KP) model (Jackson et al., 2001) and a CRISPR-Cas9-induced model driven by a chromosomal inversion resulting in the formation of the *Eml4-Alk* (EA) gene fusion (Maddalo et al., 2014). These two mouse models recapitulate two types of NSCLC observed in humans and differ not only in the initiating genetic lesions but also in the modality with which tumor formation is induced.

We generated HEAP libraries from *Ago2*$^{Halo\text{-}LSL/+}$ mice bearing primary KP (n = 2) and EA (n = 3) tumors. Tumor-specific expression of the Halo-Ago2 allele was induced at the time of tumor initiation by intratracheal delivery of Ad-Cre, alone for the KP model or in combination with recombinant adenoviruses expressing Cas9 and the two sgRNAs necessary to induce the *Eml4-Alk* rearrangement in the EA model (Ad-EA). In parallel, we also generated HEAP libraries from the lungs of two *Ago2*$^{Halo/+}$ mice (Figure 5A).

The tumor libraries produced 1,899 peaks for the KP tumors and 2,127 peaks for the EA tumors. In contrast, only 417 peaks were identified in normal lungs (Figure 5B). This difference could not be attributed to differences in sequencing depth or Halo-Ago2 expression levels in normal lungs versus tumors (Figure S5B). Rather, it may reflect reduced levels of fully assembled miRISC in the normal lung compared to lung tumors (La Rocca et al., 2015; G.L.R., unpublished data).

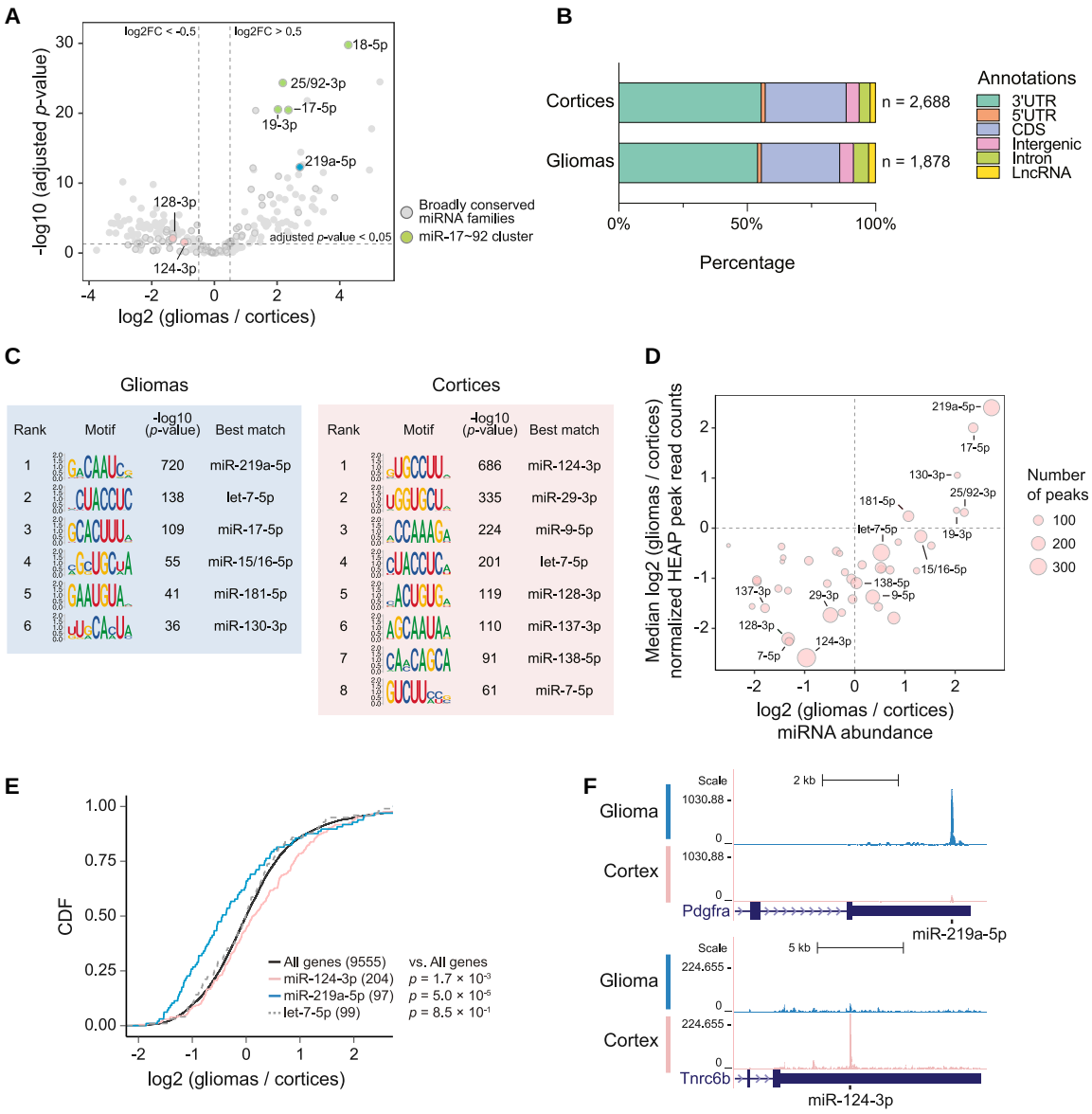

Figure 4. Mapping miRNA-Target Interactions in Normal Brain and Brain Tumors

(A) Volcano plot of global changes in miRNA family expression between normal cortices and Bcan-Ntrk1-driven gliomas, as determined by HEAP. Broadly conserved families are highlighted in circles, and a few miRNA families of interest are colored and annotated.

(B) Total number and distribution across genomic annotations of peaks identified in the cortex and glioma HEAP libraries at adjusted p value < 0.05.

(C) Top differentially enriched 8-mers in glioma and cortex HEAP peaks (peak selection cutoff: adjusted p value < 0.05; absolute log2 (gliomas/cortices) > 0.5) by the HOMER *de novo* motif discovery algorithm. miRNA families whose seed sequences are complementary to these motifs are annotated.

(D) Changes in peak intensity correlate with changes in miRNA abundance. The area of each circle is proportional to the number of targets of each miRNA seed family as identified by HEAP. Only broadly conserved miRNA families with more than 40 HEAP targets are shown.

(E) CDF plot for targets of miR-124-3p, miR-219a-5p, and let-7-5p identified by HEAP. mRNA expression was estimated using read counts in input control libraries. The mRNA log2 fold change was calculated as gliomas versus cortices. p value, two-sided Kolmogorov-Smirnov test.

(F) Genome browser view of representative Halo-Ago2 binding sites detected exclusively in gliomas (top) or cortices (bottom).

See also Figure S5A. See Data S2 for peaks identified in gliomas and cortices.

Surprisingly, a direct comparison of the peaks identified in KP and EA tumors revealed strong similarity between the two tumor types (Figures 5C, S5C, and S5D), suggesting that the miRNA targeting landscape is largely independent from the cancer initiation events in these two NSCLC models. Unbiased k-mer frequency analysis visualized as motif enrichment identified distinct miRNA seed matches enriched in peaks in normal lungs and tumors. Binding sites for let-7-5p, miR-29-3p, and miR-30-5p were strongly enriched in both tissues, while seed matches for several miRNAs implicated in tumorigenesis and metastasis,

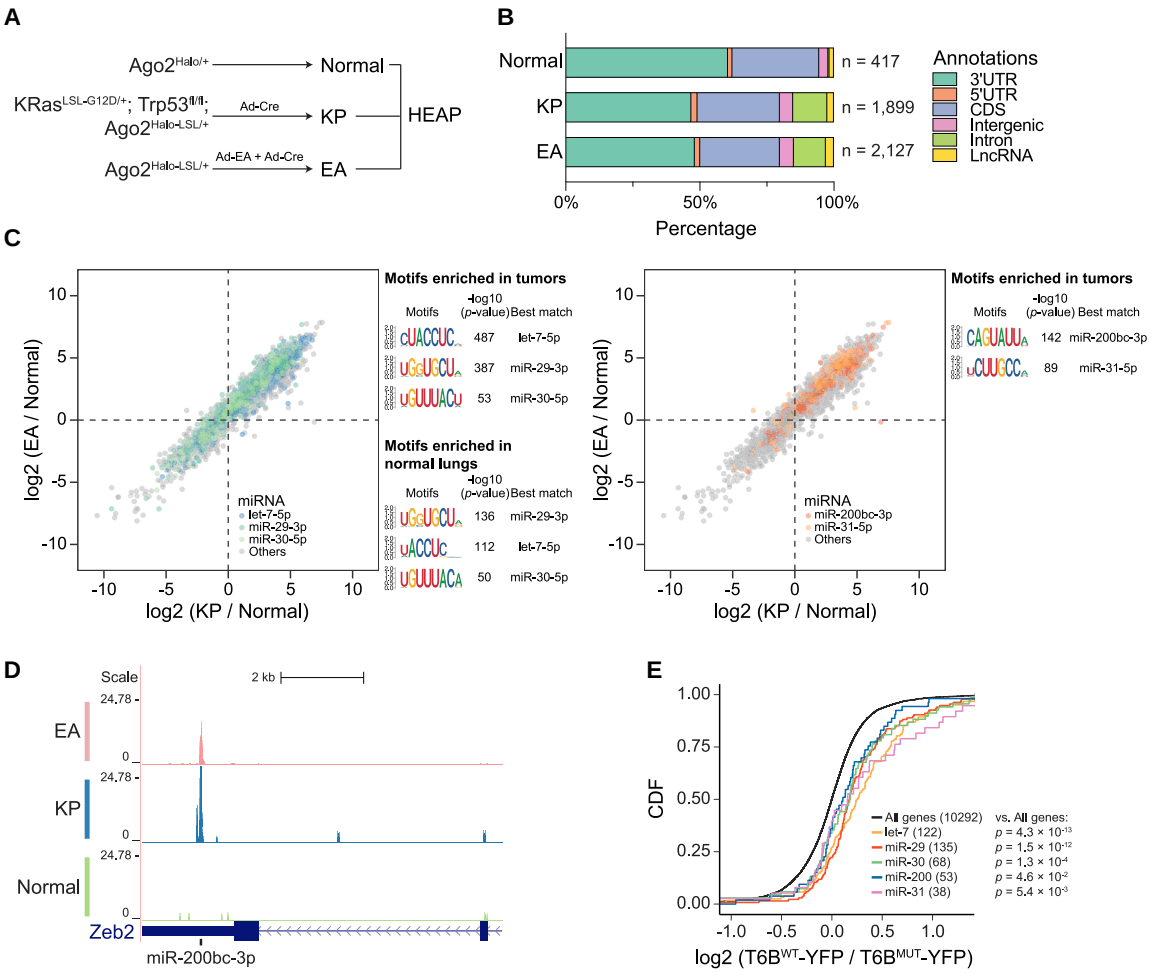

Figure 5. Mapping miRNA-Target Interactions in Lung Adenocarcinomas

(A) Schematic of the experimental design.

(B) Total number and distribution across genomic annotations of peaks identified in normal lungs (two replicates) and in the KP and EA lung adenocarcinomas (two and three replicates, respectively) at adjusted p value < 0.05.

(C) Scatterplots to compare peak intensity changes in EA versus normal (y axis) and KP versus normal (x axis). Peaks with seed matches for indicated miRNA families are colored. Left: highlighted are peaks containing seed matches for representative miRNA families whose targets were found in both normal lungs and lung adenocarcinomas. Right: highlighted are peaks with seed matches for miRNA families whose targets were preferentially found in lung adenocarcinomas. Selected motifs and their p values as determined by the HOMER *de novo* motif discovery algorithm are shown on the side.

(D) Genome browser view of the miR-200bc-3p binding site in the 3′ UTR of *Zeb2*.

(E) Targets identified by HEAP show preferential de-repression upon inactivation of the miRISC. CDF plot of mRNA expression changes induced by T6B-YFP expression in murine KP cells ($T6B^{WT}$-YFP / $T6B^{MUT}$-YFP). Targets identified by HEAP for the indicated miRNA families were compared to background ("all genes"). p value, two-sided Kolmogorov-Smirnov test.

See also Figures S5B–S5E. See Data S2 for peaks identified in normal lungs and lung adenocarcinomas.

such as miR-200bc-3p (Davalos et al., 2012; Gibbons et al., 2009; Gregory et al., 2008; Sato et al., 2017; Si et al., 2017), miR-31-5p (Edmonds et al., 2016), miR-17-5p (He et al., 2005; Ota et al., 2004), and miR-25/92-3p (Ota et al., 2004), were dominant in the tumor libraries (Figures 5C and S5E). In human lung adenocarcinomas, miR-200 levels negatively correlate with tumor metastatic potential, at least in part because this miRNA can potently suppress epithelial-to-mesenchymal transition (EMT) (Davalos et al., 2012; Gibbons et al., 2009; Si et al., 2017). In agreement with this model, we observed a strong miR-200bc-3p binding site in the 3′ UTR of *Zeb2*, a master regulator of EMT (Figure 5D).

To further validate the functional significance of these miRNA-mRNA interactions in lung cancer, we took advantage of a fusion protein (T6B-YFP) previously shown to bind Argonaute proteins and disrupt assembly of the miRISC, leading to a global de-repression of miRNA targets (Hauptmann et al., 2015; Pfaff et al., 2013; G.L.R., unpublished data). We compared the transcriptome of mouse KP cancer cells expressing either T6B-YFP ($T6B^{WT}$-YFP) or a mutant version ($T6B^{MUT}$-YFP) that cannot bind Argonaute proteins and is therefore inactive. As shown in

Figure 5E, genes harboring peaks identified by HEAP were preferentially de-repressed upon disruption of the miRISC, further confirming the ability of the HEAP method to identify functional miRNA-mRNA interactions *in vivo*.

DISCUSSION

We have demonstrated the ability of HEAP to identify miRNA-mRNA interaction sites in cells, developing embryos, normal adult tissues, and primary autochthonous tumors. By mapping miRNA binding sites in mouse embryos lacking the miR-17∼92 cluster, we identified direct targets of the miRNAs encoded by this cluster, including a long non-coding RNA that had not been previously reported to be regulated by this cluster. The HEAP method also allowed us to identify miRNA targets in primary autochthonous cancers in mice and their tissues of origin, uncovering marked differences in the spectrum of miRNA targets between cancers and normal tissues.

When compared to standard immunoprecipitation-based approaches, HEAP offers several advantages. First, the covalent nature of the interaction between the HaloTag and the HaloTag ligands simplifies the isolation of Ago2-miRNA-mRNA complexes and removes the intrinsic variability of immunoprecipitation-based approaches. This feature is illustrated by the highly reproducible identification of miRNA binding sites in mESCs, developing embryos, murine tissues, and tumors. Second, the conditional Cre-*loxP*-based nature of the Halo-Ago2 mouse strain enables the purification of Ago2-containing complexes and the identification of miRNA-mRNA interaction sites from a specific subset of cells, thus bypassing the need for microdissection and cell purification using cell surface markers. As proof of concept, we demonstrate this ability by mapping miRNA-mRNA interactions in three mouse models of human cancers driven by distinct combinations of oncogenes and tumor suppressor genes. We predict that the systematic application of HEAP will allow the construction of a detailed map of miRNA targets across tissues and cell types in mice.

We emphasize that the HEAP protocol can be easily modified to accommodate the many variations of the basic HITS-CLIP strategy, including those using ligation to generate chimeric reads between the mature miRNA and its target (crosslinking, ligation, and sequencing of hybrids [CLASH] and CLEAR-CLIP) and those designed to identify the crosslinking site at single-base resolution (photoactivatable-ribonucleoside-enhanced crosslinking and immunoprecipitation [PAR-CLIP], iCLIP, and eCLIP).

Although in this study we have focused exclusively on the identification of miRNA-mRNA interactions in cells and tissues, the conditional Halo-Ago2 mouse strain we have developed could prove useful for the biochemical characterization of Ago2-containing protein complexes *in vivo* and for imaging studies (Figure S3H; Data S1). Notably, fluorescent HaloTag ligands have been successfully used recently for super-resolution imaging of Halo-tagged proteins (Grimm et al., 2015). When applied to cells and tissues expressing the Halo-Ago2 knockin allele, this strategy could provide insights into the subcellular localization and dynamics of this important RNA binding protein under different conditions and in response to external and internal cues.

Despite these advantages, some limitations of the HEAP method should be considered when planning experiments. First, as is true for any tagged protein, the presence of the HaloTag may have functional consequences. The reduced viability of the Halo-Ago2 homozygous animal we have observed does indicate that Halo-Ago2 is not entirely functionally identical to Ago2, perhaps due to reduced stability or to a subtle impairment of miRISC assembly and activity. Thus, it will be important to experimentally evaluate the functional relevance of individual miRNA-mRNA interactions identified using this approach. Second, although the conditional nature of the Halo-Ago2 allele is ideally suited for the direct identification of miRNA targets in rare cell populations within a tissue, the HEAP method requires a relatively large number of cells (ideally 1×10^7 cells or more) to produce robust results, and in some cases, it may be therefore necessary to pool tissues from multiple animals.

In conclusion, the HEAP method and the Cre-inducible Halo-Ago2 mouse strain described in this paper, combined with the growing array of strains expressing Cre in a temporally and spatially restricted fashion, will facilitate the generation of detailed maps of miRNA-mRNA interactions *in vivo* under physiological and pathological conditions.

STAR★METHODS

Detailed methods are provided in the online version of this paper and include the following:

- KEY RESOURCES TABLE
- RESOURCE AVAILABILITY
  - Lead Contact
  - Materials Availability
  - Data and Code Availability
- EXPERIMENTAL MODEL AND SUBJECT DETAILS
  - Animal models
  - Cells lines and cell culture conditions
- METHOD DETAILS
  - Luciferase Assay
  - mESC mutagenesis
  - Protein analysis by mass spectrometry
  - Halo-Ago2 imaging
  - Size exclusion chromatography
  - Isolation of Halo-Ago2/Tnrc6 complexes
  - Dual-luciferase reporter assay
  - Two-color fluorescent reporter assay
  - Recombinant adenovirus delivery
  - T6B peptide
  - RNA sequencing
  - Analysis of public datasets
  - Z-score calculation
  - HEAP and input control library preparation
  - HEAP library preprocessing
  - Peak calling
  - miRNA abundance estimates
  - mRNA abundance estimates

- Motif discovery
- IDR analysis
- HEAP coverage analysis

- QUANTIFICATION AND STATISTICAL ANALYSIS

SUPPLEMENTAL INFORMATION

Supplemental Information can be found online at https://doi.org/10.1016/j.molcel.2020.05.009.

ACKNOWLEDGMENTS

We acknowledge the use of the Integrated Genomics Operation Core, which is funded by NCI Cancer Center Support Grant (CCSG) P30 CA08748, Cycle for Survival, and the Marie-Josée and Henry R. Kravis Center for Molecular Oncology. This work was funded by grants from the NIH (NCI R01CA149707, A.V.), the Pershing Square Sohn Cancer Research Alliance (A.V.), the Starr Cancer Consortium (A.V. and D.B.), and the Geoffrey Beene Cancer Research Foundation (A.V.). Y.P. was supported by an AACR-Bristol-Myers Squibb immuno-oncology research fellowship (grant 19-40-15-PRIT). C.P.C. was supported by NCI F31 training grant 1F31CA168356-01A1.

We thank Gregory Hannon for suggesting the use of the HaloTag to pull down Argonaute-containing complexes; Joana de Campos Vidigal for assistance with the design of the Halo-Ago2 targeting construct and gene targeting experiments; and members of the Ventura, Leslie, and Benezra laboratories for discussion and suggestions.

AUTHOR CONTRIBUTIONS

Conceptualization, A.V. and C.S.L.; Methodology, X.L., C.P.C., Y.P., P.J.C., G.L.R., Y.L., K.M.H., D.B., A.V., and C.S.L.,; Investigation, X.L, C.P.C., G.L.R., M.Z., B.K., P.J.C., Y.W.A., O.P., J.A.P., H.G.O., and R.S.; Formal Analysis and Software, Y.P., X.L., A.V., C.S.L., Y.L., and D.B.; Writing – Original Draft, X.L., C.P.C., Y.P., C.S.L., and A.V.; Writing – Review & Editing, X.L., C.P.C., Y.P., C.S.L., and A.V.; Funding Acquisition, A.V., C.S.L., D.B., and K.M.H.; Resources, P.O. and C.M.; Supervision, K.M.H., A.V., and C.S.L.

DECLARATION OF INTERESTS

The authors declare no competing interests.

Received: October 8, 2019
Revised: March 18, 2020
Accepted: May 6, 2020
Published: June 3, 2020

REFERENCES

Agarwal, V., Bell, G.W., Nam, J.-W., and Bartel, D.P. (2015). Predicting effective microRNA target sites in mammalian mRNAs. eLife *4*, e05005.

Akalin, A., Franke, V., Vlahoviček, K., Mason, C.E., and Schübeler, D. (2015). Genomation: a toolkit to summarize, annotate and visualize genomic intervals. Bioinformatics *31*, 1127–1129.

Bak, M., Silahtaroglu, A., Møller, M., Christensen, M., Rath, M.F., Skryabin, B., Tommerup, N., and Kauppinen, S. (2008). MicroRNA expression in the adult mouse central nervous system. RNA *14*, 432–444.

Bartel, D.P. (2009). MicroRNAs: target recognition and regulatory functions. Cell *136*, 215–233.

Bartel, D.P. (2018). Metazoan MicroRNAs. Cell *173*, 20–51.

Bosson, A.D., Zamudio, J.R., and Sharp, P.A. (2014). Endogenous miRNA and target concentrations determine susceptibility to potential ceRNA competition. Mol. Cell *56*, 347–359.

Chi, S.W., Zang, J.B., Mele, A., and Darnell, R.B. (2009). Argonaute HITS-CLIP decodes microRNA-mRNA interaction maps. Nature *460*, 479–486.

Cong, L., Ran, F.A., Cox, D., Lin, S., Barretto, R., Habib, N., Hsu, P.D., Wu, X., Jiang, W., Marraffini, L.A., and Zhang, F. (2013). Multiplex genome engineering using CRISPR/Cas systems. Science *339*, 819–823.

Cook, P.J., Thomas, R., Kannan, R., de Leon, E.S., Drilon, A., Rosenblum, M.K., Scaltriti, M., Benezra, R., and Ventura, A. (2017). Somatic chromosomal engineering identifies BCAN-NTRK1 as a potent glioma driver and therapeutic target. Nat. Commun. *8*, 15987.

Davalos, V., Moutinho, C., Villanueva, A., Boque, R., Silva, P., Carneiro, F., and Esteller, M. (2012). Dynamic epigenetic regulation of the microRNA-200 family mediates epithelial and mesenchymal transitions in human tumorigenesis. Oncogene *31*, 2062–2074.

Davis, S., and Meltzer, P.S. (2007). GEOquery: a bridge between the Gene Expression Omnibus (GEO) and BioConductor. Bioinformatics *23*, 1846–1847.

Dobin, A., Davis, C.A., Schlesinger, F., Drenkow, J., Zaleski, C., Jha, S., Batut, P., Chaisson, M., and Gingeras, T.R. (2013). STAR: ultrafast universal RNA-seq aligner. Bioinformatics *29*, 15–21.

Dugas, J.C., Cuellar, T.L., Scholze, A., Ason, B., Ibrahim, A., Emery, B., Zamanian, J.L., Foo, L.C., McManus, M.T., and Barres, B.A. (2010). Dicer1 and miR-219 Are required for normal oligodendrocyte differentiation and myelination. Neuron *65*, 597–611.

Edmonds, M.D., Boyd, K.L., Moyo, T., Mitra, R., Duszynski, R., Arrate, M.P., Chen, X., Zhao, Z., Blackwell, T.S., Andl, T., and Eischen, C.M. (2016). MicroRNA-31 initiates lung tumorigenesis and promotes mutant KRAS-driven lung cancer. J. Clin. Invest. *126*, 349–364.

Elias, J.E., and Gygi, S.P. (2007). Target-decoy search strategy for increased confidence in large-scale protein identifications by mass spectrometry. Nat. Methods *4*, 207–214.

Emery, B. (2010). Regulation of oligodendrocyte differentiation and myelination. Science *330*, 779–782.

Encell, L.P., Friedman Ohana, R., Zimmerman, K., Otto, P., Vidugiris, G., Wood, M.G., Los, G.V., McDougall, M.G., Zimprich, C., Karassina, N., et al. (2012). Development of a dehalogenase-based protein fusion tag capable of rapid, selective and covalent attachment to customizable ligands. Curr. Chem. Genomics *6*, 55–71.

Eng, J.K., McCormack, A.L., and Yates, J.R. (1994). An approach to correlate tandem mass spectral data of peptides with amino acid sequences in a protein database. J. Am. Soc. Mass Spectrom. *5*, 976–989.

Fan, H.B., Chen, L.X., Qu, X.B., Ren, C.L., Wu, X.X., Dong, F.X., Zhang, B.L., Gao, D.S., and Yao, R.Q. (2017). Transplanted miR-219-overexpressing oligodendrocyte precursor cells promoted remyelination and improved functional recovery in a chronic demyelinated model. Sci. Rep. *7*, 41407.

Flemr, M., and Bühler, M. (2015). Single-step generation of conditional knockout mouse embryonic stem cells. Cell Rep. *12*, 709–716.

Friedman, R.C., Farh, K.K., Burge, C.B., and Bartel, D.P. (2009). Most mammalian mRNAs are conserved targets of microRNAs. Genome Res. *19*, 92–105.

Gibbons, D.L., Lin, W., Creighton, C.J., Rizvi, Z.H., Gregory, P.A., Goodall, G.J., Thilaganathan, N., Du, L., Zhang, Y., Pertsemlidis, A., and Kurie, J.M. (2009). Contextual extracellular cues promote tumor cell EMT and metastasis by regulating miR-200 family expression. Genes Dev. *23*, 2140–2151.

Gregory, P.A., Bert, A.G., Paterson, E.L., Barry, S.C., Tsykin, A., Farshid, G., Vadas, M.A., Khew-Goodall, Y., and Goodall, G.J. (2008). The miR-200 family and miR-205 regulate epithelial to mesenchymal transition by targeting ZEB1 and SIP1. Nat. Cell Biol. *10*, 593–601.

Grimm, J.B., English, B.P., Chen, J., Slaughter, J.P., Zhang, Z., Revyakin, A., Patel, R., Macklin, J.J., Normanno, D., Singer, R.H., et al. (2015). A general method to improve fluorophores for live-cell and single-molecule microscopy. Nat. Methods *12*, 244–250.

Grimson, A., Farh, K.K., Johnston, W.K., Garrett-Engele, P., Lim, L.P., and Bartel, D.P. (2007). MicroRNA targeting specificity in mammals: determinants beyond seed pairing. Mol. Cell *27*, 91–105.

Grosswendt, S., Filipchyk, A., Manzano, M., Klironomos, F., Schilling, M., Herzog, M., Gottwein, E., and Rajewsky, N. (2014). Unambiguous identification

of miRNA:target site interactions by different types of ligation reactions. Mol. Cell *54*, 1042–1054.

Gu, J., Wang, M., Yang, Y., Qiu, D., Zhang, Y., Ma, J., Zhou, Y., Hannon, G.J., and Yu, Y. (2018). GoldCLIP: gel-omitted ligation-dependent CLIP. Genomics Proteomics Bioinformatics *16*, 136–143.

Hafner, M., Landthaler, M., Burger, L., Khorshid, M., Hausser, J., Berninger, P., Rothballer, A., Ascano, M., Jr., Jungkamp, A.C., Munschauer, M., et al. (2010). Transcriptome-wide identification of RNA-binding protein and microRNA target sites by PAR-CLIP. Cell *141*, 129–141.

Han, Y.C., Vidigal, J.A., Mu, P., Yao, E., Singh, I., González, A.J., Concepcion, C.P., Bonetti, C., Ogrodowski, P., Carver, B., et al. (2015). An allelic series of miR-17 ~ 92-mutant mice uncovers functional specialization and cooperation among members of a microRNA polycistron. Nat. Genet. *47*, 766–775.

Hauptmann, J., Schraivogel, D., Bruckmann, A., Manickavel, S., Jakob, L., Eichner, N., Pfaff, J., Urban, M., Sprunck, S., Hafner, M., et al. (2015). Biochemical isolation of Argonaute protein complexes by Ago-APP. Proc. Natl. Acad. Sci. USA *112*, 11841–11845.

He, L., Thomson, J.M., Hemann, M.T., Hernando-Monge, E., Mu, D., Goodson, S., Powers, S., Cordon-Cardo, C., Lowe, S.W., Hannon, G.J., and Hammond, S.M. (2005). A microRNA polycistron as a potential human oncogene. Nature *435*, 828–833.

Heinz, S., Benner, C., Spann, N., Bertolino, E., Lin, Y.C., Laslo, P., Cheng, J.X., Murre, C., Singh, H., and Glass, C.K. (2010). Simple combinations of lineage-determining transcription factors prime cis-regulatory elements required for macrophage and B cell identities. Mol. Cell *38*, 576–589.

Helwak, A., Kudla, G., Dudnakova, T., and Tollervey, D. (2013). Mapping the human miRNA interactome by CLASH reveals frequent noncanonical binding. Cell *153*, 654–665.

Hsin, J.P., Lu, Y., Loeb, G.B., Leslie, C.S., and Rudensky, A.Y. (2018). The effect of cellular context on miR-155-mediated gene regulation in four major immune cell types. Nat. Immunol. *19*, 1137–1145.

Huttlin, E.L., Jedrychowski, M.P., Elias, J.E., Goswami, T., Rad, R., Beausoleil, S.A., Villén, J., Haas, W., Sowa, M.E., and Gygi, S.P. (2010). A tissue-specific atlas of mouse protein phosphorylation and expression. Cell *143*, 1174–1189.

Jackson, E.L., Willis, N., Mercer, K., Bronson, R.T., Crowley, D., Montoya, R., Jacks, T., and Tuveson, D.A. (2001). Analysis of lung tumor initiation and progression using conditional expression of oncogenic K-ras. Genes Dev. *15*, 3243–3248.

Kent, W.J., Zweig, A.S., Barber, G., Hinrichs, A.S., and Karolchik, D. (2010). BigWig and BigBed: enabling browsing of large distributed datasets. Bioinformatics *26*, 2204–2207.

Kim, S.-Y., and Volsky, D.J. (2005). PAGE: parametric analysis of gene set enrichment. BMC Bioinformatics *6*, 144.

Kim, D., Paggi, J.M., Park, C., Bennett, C., and Salzberg, S.L. (2019). Graph-based genome alignment and genotyping with HISAT2 and HISAT-genotype. Nat. Biotechnol. *37*, 907–915.

Kleaveland, B., Shi, C.Y., Stefano, J., and Bartel, D.P. (2018). A network of noncoding regulatory RNAs acts in the mammalian brain. Cell *174*, 350–362.e17.

König, J., Zarnack, K., Rot, G., Curk, T., Kayikci, M., Zupan, B., Turner, D.J., Luscombe, N.M., and Ule, J. (2010). iCLIP reveals the function of hnRNP particles in splicing at individual nucleotide resolution. Nat. Struct. Mol. Biol. *17*, 909–915.

Kozomara, A., Birgaoanu, M., and Griffiths-Jones, S. (2019). miRBase: from microRNA sequences to function. Nucleic Acids Res. *47* (D1), D155–D162.

La Rocca, G., Olejniczak, S.H., González, A.J., Briskin, D., Vidigal, J.A., Spraggon, L., DeMatteo, R.G., Radler, M.R., Lindsten, T., Ventura, A., et al. (2015). In vivo, Argonaute-bound microRNAs exist predominantly in a reservoir of low molecular weight complexes not associated with mRNA. Proc. Natl. Acad. Sci. USA *112*, 767–772.

Landgraf, P., Rusu, M., Sheridan, R., Sewer, A., Iovino, N., Aravin, A., Pfeffer, S., Rice, A., Kamphorst, A.O., Landthaler, M., et al. (2007). A mammalian microRNA expression atlas based on small RNA library sequencing. Cell *129*, 1401–1414.

Langmead, B., and Salzberg, S.L. (2012). Fast gapped-read alignment with Bowtie 2. Nat. Methods *9*, 357–359.

Li, H., Handsaker, B., Wysoker, A., Fennell, T., Ruan, J., Homer, N., Marth, G., Abecasis, G., and Durbin, R.; 1000 Genome Project Data Processing Subgroup (2009). The Sequence Alignment/Map format and SAMtools. Bioinformatics *25*, 2078–2079.

Li, Q., Brown, J.B., Huang, H., and Bickel, P.J. (2011). Measuring reproducibility of high-throughput experiments. Ann. Appl. Stat. *5*, 1752–1779.

Lianoglou, S., Garg, V., Yang, J.L., Leslie, C.S., and Mayr, C. (2013). Ubiquitously transcribed genes use alternative polyadenylation to achieve tissue-specific expression. Genes Dev. *27*, 2380–2396.

Liao, Y., Smyth, G.K., and Shi, W. (2014). featureCounts: an efficient general purpose program for assigning sequence reads to genomic features. Bioinformatics *30*, 923–930.

Loeb, G.B., Khan, A.A., Canner, D., Hiatt, J.B., Shendure, J., Darnell, R.B., Leslie, C.S., and Rudensky, A.Y. (2012). Transcriptome-wide miR-155 binding map reveals widespread noncanonical microRNA targeting. Mol. Cell *48*, 760–770.

Los, G.V., Encell, L.P., McDougall, M.G., Hartzell, D.D., Karassina, N., Zimprich, C., Wood, M.G., Learish, R., Ohana, R.F., Urh, M., et al. (2008). HaloTag: a novel protein labeling technology for cell imaging and protein analysis. ACS Chem. Biol. *3*, 373–382.

Love, M.I., Huber, W., and Anders, S. (2014). Moderated estimation of fold change and dispersion for RNA-seq data with DESeq2. Genome Biol. *15*, 550.

Maddalo, D., Manchado, E., Concepcion, C.P., Bonetti, C., Vidigal, J.A., Han, Y.C., Ogrodowski, P., Crippa, A., Rekhtman, N., de Stanchina, E., et al. (2014). In vivo engineering of oncogenic chromosomal rearrangements with the CRISPR/Cas9 system. Nature *516*, 423–427.

Makeyev, E.V., Zhang, J., Carrasco, M.A., and Maniatis, T. (2007). The MicroRNA miR-124 promotes neuronal differentiation by triggering brain-specific alternative pre-mRNA splicing. Mol. Cell *27*, 435–448.

Marino, S., Vooijs, M., van Der Gulden, H., Jonkers, J., and Berns, A. (2000). Induction of medulloblastomas in p53-null mutant mice by somatic inactivation of Rb in the external granular layer cells of the cerebellum. Genes Dev. *14*, 994–1004.

Martin, M. (2011). Cutadapt removes adapter sequences from high-throughput sequencing reads. EMBnet J. *17*, 10–12.

McAlister, G.C., Nusinow, D.P., Jedrychowski, M.P., Wühr, M., Huttlin, E.L., Erickson, B.K., Rad, R., Haas, W., and Gygi, S.P. (2014). MultiNotch MS3 enables accurate, sensitive, and multiplexed detection of differential expression across cancer cell line proteomes. Anal. Chem. *86*, 7150–7158.

Moore, M.J., Scheel, T.K., Luna, J.M., Park, C.Y., Fak, J.J., Nishiuchi, E., Rice, C.M., and Darnell, R.B. (2015). miRNA-target chimeras reveal miRNA 3′-end pairing as a major determinant of Argonaute target specificity. Nat. Commun. *6*, 8864.

Mukherji, S., Ebert, M.S., Zheng, G.X.Y., Tsang, J.S., Sharp, P.A., and van Oudenaarden, A. (2011). MicroRNAs can generate thresholds in target gene expression. Nat. Genet. *43*, 854–859.

O'Carroll, D., Mecklenbrauker, I., Das, P.P., Santana, A., Koenig, U., Enright, A.J., Miska, E.A., and Tarakhovsky, A. (2007). A Slicer-independent role for Argonaute 2 in hematopoiesis and the microRNA pathway. Genes Dev. *21*, 1999–2004.

Olejniczak, S.H., La Rocca, G., Gruber, J.J., and Thompson, C.B. (2013). Long-lived microRNA-Argonaute complexes in quiescent cells can be activated to regulate mitogenic responses. Proc. Natl. Acad. Sci. USA *110*, 157–162.

Ota, A., Tagawa, H., Karnan, S., Tsuzuki, S., Karpas, A., Kira, S., Yoshida, Y., and Seto, M. (2004). Identification and characterization of a novel gene, C13orf25, as a target for 13q31-q32 amplification in malignant lymphoma. Cancer Res. *64*, 3087–3095.

Paulo, J.A., O'Connell, J.D., Everley, R.A., O'Brien, J., Gygi, M.A., and Gygi, S.P. (2016). Quantitative mass spectrometry-based multiplexing compares

the abundance of 5000 S. cerevisiae proteins across 10 carbon sources. J. Proteomics *148*, 85–93.

Peng, J., Schwartz, D., Elias, J.E., Thoreen, C.C., Cheng, D., Marsischky, G., Roelofs, J., Finley, D., and Gygi, S.P. (2003). A proteomics approach to understanding protein ubiquitination. Nat. Biotechnol. *21*, 921–926.

Pfaff, J., Hennig, J., Herzog, F., Aebersold, R., Sattler, M., Niessing, D., and Meister, G. (2013). Structural features of Argonaute-GW182 protein interactions. Proc. Natl. Acad. Sci. USA *110*, E3770–E3779.

Quinlan, A.R., and Hall, I.M. (2010). BEDTools: a flexible suite of utilities for comparing genomic features. Bioinformatics *26*, 841–842.

Ramírez, F., Ryan, D.P., Grüning, B., Bhardwaj, V., Kilpert, F., Richter, A.S., Heyne, S., Dündar, F., and Manke, T. (2016). deepTools2: a next generation web server for deep-sequencing data analysis. Nucleic Acids Res. *44* (W1), W160-5.

Ran, F.A., Hsu, P.D., Wright, J., Agarwala, V., Scott, D.A., and Zhang, F. (2013). Genome engineering using the CRISPR-Cas9 system. Nat. Protoc. *8*, 2281–2308.

Richner, M., Victor, M.B., Liu, Y., Abernathy, D., and Yoo, A.S. (2015). MicroRNA-based conversion of human fibroblasts into striatal medium spiny neurons. Nat. Protoc. *10*, 1543–1555.

Ritchie, M.E., Phipson, B., Wu, D., Hu, Y., Law, C.W., Shi, W., and Smyth, G.K. (2015). limma powers differential expression analyses for RNA-sequencing and microarray studies. Nucleic Acids Res. *43*, e47.

Robinson, J.T., Thorvaldsdóttir, H., Winckler, W., Guttman, M., Lander, E.S., Getz, G., and Mesirov, J.P. (2011). Integrative genomics viewer. Nat. Biotechnol. *29*, 24–26.

Rodríguez, C.I., Buchholz, F., Galloway, J., Sequerra, R., Kasper, J., Ayala, R., Stewart, A.F., and Dymecki, S.M. (2000). High-efficiency deleter mice show that FLPe is an alternative to Cre-loxP. Nat. Genet. *25*, 139–140.

Sakai, K., and Miyazaki, J.-i. (1997). A transgenic mouse line that retains Cre recombinase activity in mature oocytes irrespective of the cre transgene transmission. Biochem. Biophys. Res. Commun. *237*, 318–324.

Sanuki, R., Onishi, A., Koike, C., Muramatsu, R., Watanabe, S., Muranishi, Y., Irie, S., Uneo, S., Koyasu, T., Matsui, R., et al. (2011). miR-124a is required for hippocampal axogenesis and retinal cone survival through Lhx2 suppression. Nat. Neurosci. *14*, 1125–1134.

Sarshad, A.A., Juan, A.H., Muler, A.I.C., Anastasakis, D.G., Wang, X., Genzor, P., Feng, X., Tsai, P.F., Sun, H.W., Haase, A.D., et al. (2018). Argonaute-miRNA complexes silence target mRNAs in the nucleus of mammalian stem cells. Mol. Cell *71*, 1040–1050.e8.

Sato, H., Shien, K., Tomida, S., Okayasu, K., Suzawa, K., Hashida, S., Torigoe, H., Watanabe, M., Yamamoto, H., Soh, J., et al. (2017). Targeting the miR-200c/LIN28B axis in acquired EGFR-TKI resistance non-small cell lung cancer cells harboring EMT features. Sci. Rep. *7*, 40847.

Si, L., Tian, H., Yue, W., Li, L., Li, S., Gao, C., and Qi, L. (2017). Potential use of microRNA-200c as a prognostic marker in non-small cell lung cancer. Oncol. Lett. *14*, 4325–4330.

Tan, C.L., Plotkin, J.L., Venø, M.T., von Schimmelmann, M., Feinberg, P., Mann, S., Handler, A., Kjems, J., Surmeier, D.J., O'Carroll, D., et al. (2013). MicroRNA-128 governs neuronal excitability and motor behavior in mice. Science *342*, 1254–1258.

Ting, L., Rad, R., Gygi, S.P., and Haas, W. (2011). MS3 eliminates ratio distortion in isobaric multiplexed quantitative proteomics. Nat. Methods *8*, 937–940.

Ulitsky, I., Shkumatava, A., Jan, C.H., Sive, H., and Bartel, D.P. (2011). Conserved function of lincRNAs in vertebrate embryonic development despite rapid sequence evolution. Cell *147*, 1537–1550.

Van Nostrand, E.L., Pratt, G.A., Shishkin, A.A., Gelboin-Burkhart, C., Fang, M.Y., Sundararaman, B., Blue, S.M., Nguyen, T.B., Surka, C., Elkins, K., et al. (2016). Robust transcriptome-wide discovery of RNA-binding protein binding sites with enhanced CLIP (eCLIP). Nat. Methods *13*, 508–514.

Ventura, A., Meissner, A., Dillon, C.P., McManus, M., Sharp, P.A., Van Parijs, L., Jaenisch, R., and Jacks, T. (2004). Cre-lox-regulated conditional RNA interference from transgenes. Proc. Natl. Acad. Sci. USA *101*, 10380–10385.

Ventura, A., Young, A.G., Winslow, M.M., Lintault, L., Meissner, A., Erkeland, S.J., Newman, J., Bronson, R.T., Crowley, D., Stone, J.R., et al. (2008). Targeted deletion reveals essential and overlapping functions of the miR-17 through 92 family of miRNA clusters. Cell *132*, 875–886.

Wang, Y., Yang, F., Gritsenko, M.A., Wang, Y., Clauss, T., Liu, T., Shen, Y., Monroe, M.E., Lopez-Ferrer, D., Reno, T., et al. (2011). Reversed-phase chromatography with multiple fraction concatenation strategy for proteome profiling of human MCF10A cells. Proteomics *11*, 2019–2026.

Wang, H., Moyano, A.L., Ma, Z., Deng, Y., Lin, Y., Zhao, C., Zhang, L., Jiang, M., He, X., Ma, Z., et al. (2017). miR-219 cooperates with miR-338 in myelination and promotes myelin repair in the CNS. Dev. Cell *40*, 566–582.e5.

Yekta, S., Shih, I.H., and Bartel, D.P. (2004). MicroRNA-directed cleavage of HOXB8 mRNA. Science *304*, 594–596.

Zhao, J.J., Gjoerup, O.V., Subramanian, R.R., Cheng, Y., Chen, W., Roberts, T.M., and Hahn, W.C. (2003). Human mammary epithelial cell transformation through the activation of phosphatidylinositol 3-kinase. Cancer Cell *3*, 483–495.

Zhao, X., He, X., Han, X., Yu, Y., Ye, F., Chen, Y., Hoang, T., Xu, X., Mi, Q.S., Xin, M., et al. (2010). MicroRNA-mediated control of oligodendrocyte differentiation. Neuron *65*, 612–626.

STAR★METHODS

KEY RESOURCES TABLE

REAGENT or RESOURCE	SOURCE	IDENTIFIER
Antibodies		
Rabbit monoclonal anti-Ago2	Cell Signaling Technology	Cat#2897; Clone: C34C6; RRID: AB_2096291
Mouse monoclonal anti-β-actin	Sigma-Aldrich	Cat#A2228; Clone: AC-74; RRID: AB_476697
Mouse monoclonal anti-Tubulin	Sigma-Aldrich	Cat#T9026; Clone: DM1A; RRID: AB_477593
Mouse monoclonal anti-HaloTag	Promega	Cat#G9211; RRID: AB_2688011
Rabbit polyclonal anti-FLAG	Sigma-Aldrich	Cat#F7425; RRID: AB_439687
Rabbit polyclonal anti-GW182 (TNRC6A)	Bethyl	Cat#A302-329A; RRID: AB_1850240
Donkey anti-Rabbit IgG polyclonal antibody (IRDye 800CW)	LI-COR Biosciences	Cat#926-32213; RRID: AB_621848
Donkey anti-Mouse IgG polyclonal antibody (IRDye 680RD)	LI-COR Biosciences	Cat#926-68072; RRID: AB_10953628
Donkey anti-Rabbit IgG, HRP-conjugated	GE Healthcare	Cat#NA934; RRID: AB_772206
Sheep anti-Mouse IgG, HRP-conjugated	GE Healthcare	Cat#NA931; RRID: AB_772210
Bacterial and Virus Strains		
pAd-Cas9-EA (Ad-EA)	ViraQuest; Maddalo et al., 2014	N/A
pAd-Cas9-BN (Ad-BN)	ViraQuest; Cook et al., 2017	N/A
Ad-Cre	ViraQuest	N/A
Critical Commercial Assays		
Dual-Luciferase Reporter Assay System	Promega	Cat#E1960
RNeasy Mini Kit	QIAGEN	Cat#74104
TruSeq Stranded mRNA LT Kit	Illumina	Cat#RS-122-2102
TruSeq Stranded Total RNA LT Kit	Illumina	Cat#RS-122-1202
Chemicals, Peptides, and Recombinant Proteins		
HaloTag Ligands TMRDirect	Promega	Cat#G2991
Janelia Fluor 646 HaloTag ligand	Promega	Cat#GA1120
Janelia Fluor 549 HaloTag ligand	Promega	Cat#GA1110
Amersham ECL Western Blotting Detection Reagent	GE Healthcare	Cat#RPN2106
Odyssey Blocking Buffer (TBS)	LI-COR Biosciences	Cat#927-50003
KnockOut DMEM	GIBCO	Cat#10829018
Fetal Bovine Serum, embryonic stem cell-qualified, US origin	GIBCO	Cat#16141079
ESGRO Leukemia Inhibitory Factor (LIF)	Millipore	Cat#ESG1107
Penicillin-Streptomycin (5,000 U/mL)	GIBCO	Cat#15070063
GlutaMax Supplement	GIBCO	Cat#35050061
MEM non-essential amino acid solution (100X)	Sigma-Aldrich	Cat#M7145
EmbryoMax Nucleosides (100X)	Millipore	Cat#ES-008-D
2-Mercaptoethanol	BIO-RAD	Cat#1610710, CAS: 60-24-2
DMEM	GIBCO	Cat#11965118
DMEM, no phenol red	GIBCO	Cat#21063029
Advanced DMEM/F12	GIBCO	Cat#12634028
HEPES (1M)	GIBCO	Cat#15630080
Geneticin Selective Antibiotic (G418 Sulfate)	GIBCO	Cat#10131035
Halolink Resin	Promega	Cat#G1914
Magne HaloTag Beads	Promega	Cat#G7282

(*Continued on next page*)

Continued

REAGENT or RESOURCE	SOURCE	IDENTIFIER
PhosStop, Phosphatase inhibitor	Roche	Cat#4906837001
cOmplete, Mini, EDTA-free Protease Inhibitor Cocktail	Roche	Cat#11836170001
AcTEV protease	Invitrogen	Cat#12575015
Protease Inhibitor Cocktail, 50x	Promega	Cat#G6521
RQ1 RNase-Free DNase	Promega	Cat#M6101
RNase A	Affymetrix	Cat#70194Z
Alkaline Phosphatase, Calf Intestinal (CIAP)	Promega	Cat#M1821
T4 RNA Ligase 1	New England Biolabs	Cat#M0204
T4 Polynucleotide Kinase	New England Biolabs	Cat#M0201
SuperScript III Reverse Transcriptase	Invitrogen	Cat#18080044
Accuprime Pfx Supermix	Invitrogen	Cat#12344040
Proteinase K, recombinant, PCR Grade	Roche	Cat#3115836001
Phenol solution	Sigma-Aldrich	Cat#P4682
Chloroform – isoamyl alcohol mixture	Sigma-Aldrich	Cat#25668
Novex TBE-Urea Gels, 15%, 10 well	Invitrogen	Cat#EC6885BOX
Novex TBE Gels, 6%, 10 well	Invitrogen	Cat#EC6265BOX
SYBR Green I Nucleic Acid Gel Stain	Invitrogen	Cat#S7563
Dynabeads MyOne Silane	ThermoFisher Scientific	Cat#37002D
TRIzol Reagent	Invitrogen	Cat#15596026
RNase-Free DNase Set	QIAGEN	Cat#79254
NEBuilder HiFi DNA Assembly Master Mix	New England Biolabs	Cat#E2621L
cOmplete Protease Inhibitor Cocktail (Mass Spectrometry)	Roche	Cat#11836153001
Trypsin Gold, Mass Spectrometry Grade	Promega	Cat#V5280
Lysyl Endopeptidase (Lys-C)	Wako Chemicals	Cat#129-02541
TMT10plex Isobaric Label Reagent Set plus TMT11-131C Label Reagent	Thermo Fisher Scientific	Cat#A34808
Oligonucleotides		
See Table S1	N/A	N/A
Deposited Data		
HEAP libraries and RNA-seq datasets	This paper	GSE139349
TT-FHAgo2 mESC iCLIP	Bosson et al., 2014	GSE61348
TT-FHAgo2 mESC RNaseq	Bosson et al., 2014	GSE61348
CLEAR-CLIP	Moore et al., 2015	GSE73059
miR-17~92 E9.5 embryo RNA-seq	Han et al., 2015	GSE63813
miR-124 overexpression CAD	Makeyev et al., 2007	GSE8498
miRbase version 21	Kozomara et al., 2019	ftp://mirbase.org/pub/mirbase/21/
TargetScan	Agarwal et al., 2015	http://www.targetscan.org/mmu_71/mmu_71_data_download/miR_Family_Info.txt.zip
Experimental Models: Cell Lines		
Ago2$^{-/-}$ MEFs	Alexander Tarakhovsky Laboratory; O'Carroll et al., 2007	N/A
Ago2$^{Halo\text{-}LSL/+}$ mESCs	This paper	N/A
Ago2$^{Halo/+}$ mESCs	This paper	N/A
Ago2$^{Halo\text{-}LSL}$ MEFs	This paper	N/A
Ago2^{Halo} MEFs	This paper	N/A
KRas^{G12D};*Trp53*$^{-/-}$ (KP) NSCLC cell lines	This paper	N/A
V6.5 mESCs	Rudolf Jaenisch Laboratory	N/A

(*Continued on next page*)

Continued

REAGENT or RESOURCE	SOURCE	IDENTIFIER
Experimental Models: Organisms/Strains		
Mouse: *KRas$^{LSL-G12D/+}$: B6.129S4-Kras^{tm4Tyj}/J*	Jackson et al., 2001	JAX Stock No. 008179
Mouse: *Trp53$^{fl/fl}$: B6.129P2-Trp53^{tm1Brn}/J*	Marino et al., 2000	JAX Stock No. 008462
Mouse: *β-actin-Flpe: B6;SJL-Tg(ACTFLPe)9205Dym/J*	Memorial Sloan Kettering Cancer Center Mouse Genetics Core Facility; Rodríguez et al., 2000	JAX Stock No. 003800
Mouse: *CAG-Cre: Tg(CAG-cre)13Miya*	Memorial Sloan Kettering Cancer Center Mouse Genetics Core Facility; Sakai and Miyazaki, 1997	N/A
Mouse: *Ago2$^{Halo-LSL}$*	This paper	N/A
Mouse: *Ago2^{Halo}*	This paper	N/A
Mouse: *miR-17~92$^{-/-}$*	Ventura et al., 2008	N/A
Recombinant DNA		
MSCV-PIG-Empty	Addgene	Addgene: 18751
MSCV-PIG-Halo	This paper	N/A
MSCV-PIG-Ago2	This paper	N/A
MSCV-PIG-Halo-Ago2	This paper	N/A
pKOII-Halo-lox-IRES-lox-Ago2	This paper	N/A
pMB1610_pRR-puro	Flemr and Bühler, 2015	Addgene: 65853
PX330	Cong et al., 2013; Ran et al., 2013	Addgene: 42230
PX333	Maddalo et al., 2014	Addgene: 64073
piS0	Yekta et al., 2004	Addgene: 12178
piS1	Addgene	Addgene: 12179
psico luc + Cre	Ventura et al., 2004	N/A
psico CD8 + Cre	Ventura et al., 2004	N/A
pBABE-SV40-puro	Zhao et al., 2003	Addgene:13970
pTRETightBI-RY-0	Mukherji et al., 2011	Addgene: 31463
pTRETightBI-RY-1pf	Mukherji et al., 2011	Addgene: 31467
pTRETightBI-RY-4	Mukherji et al., 2011	Addgene: 31465
rtTA-N144	Richner et al., 2015	Addgene: 66810
psiCheck2	Promega	C8021
psiCheck2-Pten-miR-29-WT	This paper	N/A
psiCheck2-Pten-miR-29-MUT	This paper	N/A
psiCheck2-Adrb2-let-7-WT	This paper	N/A
psiCheck2-Adrb2-let-7-MUT	This paper	N/A
psiCheck2-Taf7-miR-21-WT	This paper	N/A
psiCheck2-Taf7-miR-21-MUT	This paper	N/A
Turn-T6B^{WT}-EYFP	This paper	N/A
Turn-T6B^{MUT}-EYFP	This paper	N/A
Software and Algorithms		
STAR (v2.5.3a)	Dobin et al., 2013	https://github.com/alexdobin/STAR
Cutadapt (v1.15 and v1.17)	Martin, 2011	https://cutadapt.readthedocs.io/en/stable/
Bowtie2 (v2.3.4)	Langmead and Salzberg, 2012	http://bowtie-bio.sourceforge.net/bowtie2
DESeq2 (v1.20.0, v1.6.3 and 1.22.1)	Love et al., 2014	https://bioconductor.org/packages/release/bioc/html/DESeq2.html
IDR	Li et al., 2011	https://github.com/nboley/idr
Deeptools (v3.1.3)	Ramírez et al., 2016	https://deeptools.readthedocs.io/en/develop/
Bedtools (v2.23.0)	Quinlan and Hall, 2010	https://bedtools.readthedocs.io/en/latest/
kentUtils	Kent et al., 2010	https://github.com/ENCODE-DCC/kentUtils

(*Continued on next page*)

Continued

REAGENT or RESOURCE	SOURCE	IDENTIFIER
Limma (v3.38.3)	Ritchie et al., 2015	http://bioconductor.org/packages/release/bioc/html/limma.html
featureCounts (v1.6.3)	Liao et al., 2014	http://bioinf.wehi.edu.au/featureCounts
Genomation (v1.14.0)	Akalin et al., 2015	https://bioconductor.org/packages/release/bioc/html/genomation.html
HISAT2 (v0.1.6-beta)	Kim et al., 2019	http://ccb.jhu.edu/software/hisat2/
GEOquery (v2.50.5)	Davis and Meltzer, 2007	https://bioconductor.org/packages/release/bioc/html/GEOquery.html
Samtools (v1.3.1)	Li et al., 2009	http://www.htslib.org
Parametric Analysis of Gene Set Enrichment	Kim and Volsky, 2005	N/A
HOMER	Heinz et al., 2010	http://homer.ucsd.edu/homer/
CLIPanalyze (v0.0.8)	unpublished	https://bitbucket.org/leslielab/clipanalyze
Sequest	Eng et al., 1994	https://www.thermofisher.com/order/catalog/product/OPTON-30945?SID=srch-srp-OPTON-30945#/OPTON-30945?SID=srch-srp-OPTON-30945
Odyssey	LI-COR Biosciences	https://www.licor.com/bio/
IGV	Robinson et al., 2011	http://software.broadinstitute.org/software/igv/
ZEN	ZEISS	https://www.zeiss.com/microscopy/int/downloads.html
Fiji	NIH	https://imagej.net/Fiji
Other		
Superose 6 column	GE Healthcare	Cat#10/300 GL
Sep-Pak C18 3 cc Vac Cartridge, 200 mg	Waters	Cat#WAT054945

RESOURCE AVAILABILITY

Lead Contact

Further information and requests for resources and reagents should be directed to and will be fulfilled by the Lead Contact, Andrea Ventura (venturaa@mskcc.org).

Materials Availability

All unique reagents generated in this study are available from the Lead Contact with a completed Materials Transfer Agreement.

Data and Code Availability

The accession number for the datasets reported in this paper is GEO: GSE139349. CLIPanalyze is available for download at https://bitbucket.org/leslielab/clipanalyze. This published article includes algorithms and key parameters used during this study.

EXPERIMENTAL MODEL AND SUBJECT DETAILS

Animal models

The Halo-Ago2 conditional knock-in mice were generated through gene targeting. The targeting construct was generated by modifying the pKO-II vector through three steps of cloning. First, a fragment comprising a 2 kb 5′ homology arm, the 5′UTR of Ago2, the HaloTag cDNA, the TEV protease recognition sequence, the coding sequence of Ago2 Exon1 and a portion of the first intron was inserted into the pKO-II vector immediately upstream of the frt-PGK-NEO-frt cassette. Second, a 5 kb 3′ homology arm was cloned into the HindIII site downstream of the frt-PGK-NEO-frt casette. Lastly, a *lox*P-STOP-IRES-FLAG-*lox*P cassette was inserted into the AsiSI site between the TEV cleavage sequence and Ago2 coding sequence.

V6.5 mESCs (obtained from the Rudolf Jaenisch laboratory at Whitehead Institute and Massachusetts Institute of Technology) were electroporated with the linearized targeting construct and selected in mESC medium containing G418 (GIBCO) for 7 days. Recombinant clones were identified by Southern blot using probes designed against sequences outside the 5′ and 3′ homology regions. A validated clone was injected into C57BL/6 blastocyst to generate chimeric mice. Mice heterozygous for the targeted

allele were crossed to the *β-actin-Flpe* mice (Rodríguez et al., 2000) to remove the frt-PGK-NEO-frt cassette, resulting in the generation of *Ago2*$^{Halo\text{-}LSL/+}$ mice. The *Ago2*$^{Halo/+}$ mice were obtained by crossing the *Ago2*$^{Halo\text{-}LSL/+}$ mice to the *CAG-Cre* mice (Sakai and Miyazaki, 1997).

Mice carrying the knock-in alleles were genotyped using a three-primer PCR (p1, 5′- GCAACGCCACCATGTACTC-3′, final concentration 0.75 μM; p2, 5′- GAGGACGGAGACCCGTTG-3′, final concentration 1.0 μM; p3, 5′-AGCCGTTCCTGAATCCTGTT-3′, final concentration 0.5 μM), which amplifies a 240-bp band from the wild-type allele (p1-p2), a 1281-bp band from the *Ago2*$^{Halo\text{-}LSL}$ allele and a 651-bp band from the *Ago2*^{Halo} allele (p2-p3).

We also used *miR-17∼92*$^{-/-}$ (Ventura et al., 2008), *Trp53*$^{fl/fl}$ (Marino et al., 2000) and *KRas*$^{LSL\text{-}G12D/+}$ (Jackson et al., 2001) mice in this study. For the generation of E13.5 embryos, 6∼10-week-old females were sacrificed at embryonic day 13.5. To generate P13 cortex HEAP libraries, cortices were harvested from 13-day-old *Ago2*$^{Halo/+}$ mice. For the generation of gliomas, 4∼6-week-old *Ago2*$^{Halo\text{-}LSL/+}$*; Trp53*$^{fl/fl}$ mice were infected with recombinant adenoviruses and tumors were harvested approximately 80 days after injection. Normal cortices were harvested from age-matched *Ago2*$^{Halo/+}$ mice. For the generation of lung adenocarcinomas, 10∼12-week-old *Ago2*$^{Halo\text{-}LSL/+}$ (EA model) and *Ago2*$^{Halo\text{-}LSL/+}$*; KRas*$^{LSL\text{-}G12D/+}$*; Trp53*$^{fl/fl}$ (KP model) mice were infected with recombinant adenoviruses and tumors were harvested 3 months after infection. Normal lungs were obtained from age-matched *Ago2*$^{Halo/+}$ mice.

All studies and procedures were approved by the Memorial Sloan Kettering Cancer Center Institutional Animal Care and Use Committee.

Cells lines and cell culture conditions

Ago2^{Halo} and *Ago2*$^{Halo\text{-}LSL}$ MEFs were generated by intercrossing *Ago2*$^{Halo/+}$ and *Ago2*$^{Halo\text{-}LSL/+}$ mice, respectively and derived using standard protocols. MEFs were immortalized with retrovirus expressing the SV40 large T antigen (Addgene:13970) (Zhao et al., 2003). *Ago2*$^{-/-}$ MEFs were a kind gift from Alexander Tarakhovsky (Rockefeller University). Murine KP cells were derived from murine *KRas*^{G12D}*; Trp53*$^{-/-}$ lung adenocarcinomas.

Cells were maintained in a humidified incubator at 37°C, 5% CO_2. mESCs were grown on irradiated MEFs in KnockOut DMEM (GIBCO) supplied with 15% FBS (GIBCO), leukemia inhibitory factor (Millipore, 1000 U / mL), penicillin/streptomycin (GIBCO, 50 U/ mL), GlutaMax (GIBCO), non-essential amino acids (Sigma-Aldrich), nucleosides (Millipore) and 2-Mercaptoethanol (Bio-Rad, 100 μM). MEFs were cultured in DMEM (GIBCO) containing 10% FBS, penicillin/streptomycin (100 U/mL) and L-glutamine. KP cells were cultured in Advanced DMEM/F12 (GIBCO, 1:1) containing 5% FBS, HEPES (GIBCO, 10 mM), GlutaMax and penicillin/streptomycin (100 U/mL).

METHOD DETAILS

Luciferase Assay

Ago2$^{-/-}$ MEFs were transduced with the MSCV-PIG (Addgene: 18751), MSCV-PIG-Halo, MSCV-PIG-Halo-Ago2 or MSCV-PIG-Ago2 retroviruses to generate cell lines stably expressing HaloTag, the Halo-Ago2 fusion or Ago2. The dual-luciferase reporter assay system (Promega) was used to measure the cleavage activity of Halo-Ago2 and Ago2. Luciferase reporter plasmids pIS0 (*luc*+, Firefly luciferase, Addgene: 12178) (Yekta et al., 2004) and pIS1 (*Rluc*, Renilla luciferase, Addgene: 12179) were co-transfected into MEFs, along with a pSico vector expressing an shRNA against the Firefly luciferase or a control shRNA against CD8 (Ventura et al., 2004). The ratio between Firefly and Renilla luciferase activity was measured following manufacturer's instructions at 48 hr after transfection.

mESC mutagenesis

The Dicer1 knockout cells were generated from *Ago2*$^{Halo/+}$ mESCs using CRISPR-Cas9. A pX333 vector (Addgene: 64073) (Maddalo et al., 2014) expressing Cas9 and a pair of guide RNAs designed to delete a portion of the RNase III 1 domain of Dicer1, was transiently transfected into *Ago2*$^{Halo/+}$ mESCs. Single clones were isolated and genotyped by PCR.

Lefty2 mutant clones were generated from *Ago2*$^{Halo/+}$ mESCs using CRISPR-Cas9-mediated homologous recombination. PX330 vectors (Addgene: 42230) (Cong et al., 2013; Ran et al., 2013) expressing Cas9 and guide RNAs targeting the predicted miR-291-3p binding site in the 3′UTR of *Lefty2* were transiently transfected, together with single-stranded template DNAs, into *Ago2*$^{Halo/+}$ mESCs. Clones undergoing homologous recombination were enriched using the method developed by Flemr and Buhler with plasmid pMB1610_pRR-Puro (Addgene: 65853) containing a fragment of guide RNA target sequence (Flemr and Bühler, 2015). Clones homozygous for the desired mutations were identified by PCR and Sanger sequencing. See also Table S1 for oligo information.

Protein analysis by mass spectrometry

Tandem Mass Tag mass spectrometry

Five independent Dicer1 knockout and five wild-type mESC clones were used in the proteomic analysis. Frozen cell pellets were lysed in 8 M urea and 200 mM EPPS, pH 8.5 with protease inhibitor (Roche) and lysates were additionally passed 10 times through a 21-gauge needle. Disulfide bonds were reduced using 5 mM tris(2-carboxyethyl)phosphine (30 min, RT) and alkylated with 10 mM

iodoacetamide (30 min, RT in the dark). Alkylation reaction was quenched with 10 mM dithiotreitol for 15 min at RT. Per sample 100 μg protein (protein concentration determined prior to reduction/alkylation by BCA assay) were precipitated using methanol-chloroform precipitation and digested at RT with Lys-C protease (Wako Chemicals) in 200 mM EPPS, pH 8.5 at a 50:1 protein:enzyme ratio overnight. More complete protein digestion was achieved through addition of trypsin (100:1 protein:enzyme ratio, Promega) for an additional 6 hr at 37°C. Acetonitrile was added to sample to a concentration of approximately 30%, and peptides were labeled with 0.2 mg TMT isobaric label reagent (Thermo Fisher Scientific) per sample for 1 hr at RT. Labeling reactions were quenched with the addition of hydroxylamine to 0.3% (v/v). Samples were combined at a 1:1:1:1:1:1:1:1:1:1 ratio and dried down by vacuum centrifugation. Excess TMT label was removed by C18 solid-phase extraction (Waters). The pooled sample was fractioned by offline basic pH reversed-phase HPLC over a 50 min 5%–35% acetonitrile gradient in 10 mM ammonium bicarbonate pH 8.0 into 96 fractions using an Agilent 300Extend C18 column (Wang et al., 2011). Collected fractions were combined into 48 fractions, of which 24 non-adjacent fractions were desalted using StageTips, dried by vacuum centrifugation and peptides were solubilized in 5% acetonitrile and 5% formic acid for subsequent LC-MS/MS analysis (Paulo et al., 2016). Approximately 2 μg of each sample was analyzed on an Orbitrap Fusion Lumos mass spectrometer (Thermo Fisher Scientific) coupled to a Proxeon EASY-nLC 1200 liquid chromatography pump (Thermo Fisher Scientific) and a 100 μm × 35 cm microcapillary column packed with Accucore C18 resin (2.6 μm, 150 Å, Thermo Fisher). Peptides were fractionated over a 150 min gradient of 3 – 25% acetronitrile in 0.125% formic acid. An MS^3-based TMT method was used, as described previously (McAlister et al., 2014; Paulo et al., 2016; Ting et al., 2011). MS^1 spectra were acquired with a resolution of 120,000, 350-1400 Th, an automatic gain control (AGC) target of $5e^5$, and a maximum injection time of 100 ms in the Orbitrap mass analyzer. The ten most intense ions were fragmented by collision-induced dissociation (CID) and analyzed in a quadrupole ion trap with AGC $2e^4$, normalized collision energy (NCE) 35, q-value 0.25, maximum injection time 120 ms, and an isolation window of 0.7 Th. MS^3 spectra were acquired in the Orbitrap mass analyzer (AGC $2.5e^5$, NCE 65, maximum injection time 150 ms, 50,000 resolution at 400 Th) after fragmentation of MS2 ions by HCD. Isolation windows were chosen depended on charge state z (z = 2 1.3 Th, z = 3 1 Th, z = 4 0.8 Th, z = 5 0.7 Th).

Mass spectrometry data processing

Spectra were searched using Sequest (Eng et al., 1994) with a 50 ppm precursor mass tolerance, 0.9 fragment ion tolerance and a maximum of two internal cleavage sites. Methionine oxidation was included as a variable modification, with a maximum of three modifications per peptide. Cysteine alkylation and TMT addition on lysines and peptide N-termini were set as fixed modifications. Spectra were searched against the Uniprot mouse proteome sequence database (downloaded on February 7th, 2014) containing both SwissProt and TrEMBL entries. Common contaminants were added to the database. The database was sorted in the following order: contaminant, SwissProt entries, TrEMBL entries and protein length within each category. All peptide sequences in the database were reversed and appended. FDR was estimated by linear discriminant analysis (Elias and Gygi, 2007; Peng et al., 2003), a 1% FDR filtering was applied at the peptide and protein level. Peptides were collapsed into a minimal number of protein identification as described by Huttlin and colleagues (Huttlin et al., 2010). This resulted in a filtered matrix of protein abundance values for 8,056 proteins. Then log2FC of abundance was calculated for each protein by summing values within five replicates of each condition, adding 1 to each sum, and then taking log2 of the ratio of the sums.

Halo-Ago2 imaging

Ago2$^{-/-}$ MEFs transduced with retroviruses MSCV-PIG, MSCV-PIG-Halo or MSCV-PIG-Halo-Ago2 were treated with 100 nM HaloTag TMRDirect ligand (Promega) overnight and imaged on a ZEISS AXIO A1 microscope with AXIOCam MRC (ZEISS). A LD Plan-NEOFLUAR 20X/0.4 Ph2 korr objective was used.

Ago2$^{+/+}$, *Ago2*$^{Halo\text{-}LSL/Halo\text{-}LSL}$ and *Ago2*$^{Halo/Halo}$ MEFs were treated with 200 nM Janelia Fluor 646 HaloTag ligands or Janelia Fluor 549 HaloTag ligands (Promega) at least 1hr prior to experiment. Before imaging, medium containing HaloTag ligands was replaced with warm medium without phenol red (GIBCO). Cells were kept at 37°C with 5% CO_2 and 100% humidity while imaging. Confocal imaging was performed on a ZEISS LSM880 microscopy (Carl Zeiss) using the Airyscan module. A 63X 1.4 NA oil objective was used. Time lapse images were acquired with a Zeiss alpha Plan-Apochromat 100X/1.46NA objective on an Axio Observer.Z1 in widefield using a Hamamatsu ORCA Flash4.0 v2 camera. Interval between frames was 500 ms with 250 ms exposures. Images were processed using ZEN (Zeiss) and Fiji (NIH).

Size exclusion chromatography

Cells were lysed with Sup6-150 buffer (150 mM NaCl, 10 mM Tris-HCl, pH 7.5, 2.5 mM $MgCl_2$, 0.01% Triton X-100, protease inhibitor (Roche) and phosphatase inhibitor (Roche)). Lysates were fractionated using the Superose 6 10/300 GL prepacked column (GE Healthcare) coupled with the AKTA FPLC system as described in (La Rocca et al., 2015; Olejniczak et al., 2013). Eluted proteins were concentrated by trichloroacetic acid (TCA)/acetone precipitation, analyzed by immunoblot and imaged using the Odyssey CLx imaging system (LI-COR).

Isolation of Halo-Ago2/Tnrc6 complexes

Ago2$^{Halo\text{-}LSL/Halo\text{-}LSL}$ and *Ago2*$^{Halo/Halo}$ MEFs were lysed with HaloTag protein purification buffer (150 mM NaCl, 50 mM HEPES, pH 7.5, 0.005% IGEPAL CA-630) and lysates were incubated with HaloTag magnetic beads (Promega) for 90 min at room temperature

on a rotator. After three washes with the HaloTag protein purification buffer, proteins were released by TEV protease (Invitrogen) digestion at 30°C for 1 hr. Eluted proteins were analyzed by immunoblot and visualized using ECL (GE Healthcare).

Dual-luciferase reporter assay

Fragments of the 3′UTRs of *Pten* and *Adrb2* containing miRNA binding sites for miR-29-3p and let-7-5p, respectively, were amplified from cDNA and cloned into the multiple cloning site of the psiCHECK2 vector (Promega) by HiFi assembly (New England Biolabs). Control vectors were created by mutagenizing the predicted miRNA seed match in each of these vectors by PCR using 5′ phosphorylated primers followed by ligation. For *Taf7*, 3′UTR fragments containing wild-type or mutant binding site for miR-21-5p were synthesized and cloned into the psiCHECK2 vector by HiFi assembly. The luciferase reporters were transfected into MEFs in triplicates. Luciferase activity was measured using the dual-luciferase reporter assay system (Promega) according to manufacturer's instructions 48 hr post transfection. See also Table S1 for oligo information.

Two-color fluorescent reporter assay

MEFs were engineered to stably express the reverse tetracycline-controlled transactivator (rtTA) using a lentiviral vector rtTA-N144 (Addgene: 66810) (Richner et al., 2015). The two-color fluorescent reporter pTRETightBI-RY-0 (Addgene: 31463), pTRETightBI-RY-1pf (Addgene: 31467) and pTRETightBI-RY-4 (Addgene: 31465) were transfected into the rtTA-expressing MEFs. 48 hr after transfection, fluorescent signals were measured using flow cytometry. Signals were processed as described by Mukherji and colleagues (Mukherji et al., 2011). Mean and standard deviation of autofluorescence in eYFP and mCherry channels were obtained from untransfected cells. The mean autofluorescence plus twice the standard deviation was subtracted from each cell's eYFP and mCherry signals. Cells with eYFP signals lower than 0 were removed. The fluorescent signals were binned along the eYFP axis and mean mCherry signals were calculated in each bin.

Recombinant adenovirus delivery

Recombinant adenoviruses used for inducing chromosomal rearrangements (Ad-BN, Ad-EA) (Cook et al., 2017; Maddalo et al., 2014) and Ad-Cre were purchased from ViraQuest.

For the generation of Bcan-Ntrk1-driven gliomas, a 1:1 mixture of Ad-BN and Ad-Cre, in total ~3×10^9 infectious particles, was administrated to *Ago2*$^{Halo\text{-}LSL/+}$; *Trp53*$^{fl/fl}$ mice (4~6 weeks old), via stereotactic intracranial injection as described in Cook et al., 2017. Gliomas were harvested approximately 80 days after injection, when mice became symptomatic.

For the generation of Eml4-Alk-driven lung adenocarcinomas, 10~12-week-old *Ago2*$^{Halo\text{-}LSL/+}$ mice were intratracheally infected with a 1:1 mixture of Ad-EA and Ad-Cre (in total ~6×10^{10} infectious particles). To generate *KRas*^{G12D}; *Trp53*$^{-/-}$ lung tumors, 10~12-week-old *Ago2*$^{Halo\text{-}LSL/+}$; *KRas*$^{LSL\text{-}G12D/+}$; *Trp53*$^{fl/fl}$ mice were intratracheally infected with Ad-Cre (~2.5×10^7 PFU). Lung tumors were harvested approximately 3 months after infection.

T6B peptide

Mouse KP cells were transduced with retroviruses expressing the T6B^{WT}-YFP or the T6B^{MUT}-YFP fusion protein, in which five tryptophan residues were mutated to alanines [(Hauptmann et al., 2015; Pfaff et al., 2013) and LaRocca et al., manuscript in preparation].

RNA sequencing

Total RNAs from mESCs, MEFs, lung adenocarcinomas and normal lung tissues were extracted using TRIzol Reagent (Invitrogen) and subjected to DNase (QIAGEN) treatment followed by RNeasy column clean-up (QIAGEN). After quantification and quality control, 500 ng of total RNA underwent poly(A) selection and TruSeq library preparation using the TruSeq Stranded mRNA LT Kit (Illumina) according to the manufacturer's instructions. Samples were barcoded and run on a HiSeq 2500 or a Hiseq 4000 in a 50bp/50bp paired end run.

Total RNAs of T6B-YFP-expressing KP cells were isolated using TRIzol Reagent and subjected to DNase treatment and isopropanol re-precipitation. After quantification and quality control, 1 ug of total RNA underwent ribosomal depletion and library preparation using the TruSeq Stranded Total RNA LT Kit (Illumina). Samples were run on a HiSeq 4000 in a 50bp/50bp paired end run.

Reads were aligned to the standard mouse genome (mm10) using Hisat2 (v0.1.6-beta) (Kim et al., 2019) or STAR v2.5.3a (Dobin et al., 2013). RNA reads aligned were counted at each gene locus. Expressed genes were subjected to differential gene expression analysis by DESeq2 v1.20.0 (Love et al., 2014).

Analysis of public datasets

RNA-seq data generated from E9.5 miR-17~92 mutant embryos were obtained from the authors and are available in GEO (GEO: GSE63813) (Han et al., 2015). In this study, gene expression was profiled in triplicates in heart, mesoderm and all remaining tissues of wild-type (WT) embryos and embryos null for miR-17 and miR-20a (Δ17), null for miR-18a (Δ18), null for miR-19a and miR-19b-1 (Δ19), and null miR-92a-1 (Δ92), null for miR-17, miR-18a and miR-20a (Δ17,18), null for miR-17, miR-18a, miR-20a and miR-92a-1 (Δ17,18,92), and null for the entire cluster (KO). Embryos were of different genders. The data was aligned using HISAT v0.1.6-beta. In each tissue, differential gene expression analysis was performed using DESeq2 v1.6.3 using multi-factorial model "~ d17 + d18 + d19 + d92 + gender," where factor "d17" encoded for conditions that were Δ17, factor "d18" encoded for conditions that were

Δ18, etc., and factor "gender" encoded for the genders of the embryos. This allowed us to estimate the log2FC of expression associated with each individual miRNA family in each tissue when accounting for contribution from other miRNA families and the gender.

The microarray dataset from CAD cell expressing miR-124 was obtained from GEO: GSE8498 (Makeyev et al., 2007) using function getGEO() from GEOquery v2.50.5 (Davis and Meltzer, 2007). Differential expression analysis was run using functions lmFit() and eBayes() from limma v3.38.3 (Ritchie et al., 2015).

The TT-FHAGO2 RNA-seq, iCLIP (GEO: GSE61348) (Bosson et al., 2014), and CLEAR-CLIP (GEO: GSE73059) (Moore et al., 2015) datasets were processed and aligned to the UCSC mm10 mouse genome using STAR v2.5.3a. Reads mapping to multiple loci or with more than 5 mismatches were discarded. For TT-FHAGO2 RNA-seq, differential expression analysis was run using DESeq2 v1.20.0.

Z-score calculation

For conserved miRNA families, the mean log2-fold change of predicted targets compared to the rest of the transcriptome (background) was calculated. The means were converted to z-scores using an approach developed by Kim and Volsky (Kim and Volsky, 2005). Z-score = (Sm - μ) × $m^{1/2}$ / SD, where Sm is the mean of log2-fold changes of genes for a given gene set, m is the size of the gene set, and μ and SD are the mean and the standard deviation of background log2-fold change values.

HEAP and input control library preparation

mESCs were harvested and irradiated with UV at dose 400 mJ/cm^2 in cold PBS on ice. Fresh tissues were harvested, homogenized and irradiated with UV for three times at dose 400 mJ/cm^2. Cell or tissue pellets were snap frozen on dry-ice and stored at −80°C.

Frozen pellets were thawed, lysed with mammalian lysis buffer (50 mM Tris-HCl, pH 7.5, 150 mM NaCl, 1% Triton X-100 and 0.1% Na deoxycholate) containing protease inhibitor cocktail (Promega) and treated with RQ1 DNase (Promega) for 5 min at 37°C. In order to get the "footprint" Halo-Ago2, lysates were treated with RNase A (Affymetrix, 1:50,000 diluted in TBS) for 5 min at 37°C. ~2% of the lysates were saved for input control library preparation. The remaining lysates were diluted with buffer TBS (700 μL TBS per 300 μL lysates). For each sample, 300 μL Halolink resin (Promega) was used. The Halolink resin was equilibrated with TBS buffer containing 0.05% IGEPAL CA-630 (Wash/Eq) and incubated with the TBS-diluted lysates at room temperature for 1.5 hr. After incubation, the resin was washed extensively with a series of buffers: SDS elution buffer (50 mM Tris-HCl, pH 7.5 and 0.1% SDS, one wash for 30 min at room temperature on a rotator), LiCl wash buffer (100 mM Tris-HCl, pH 8.0, 500 mM LiCl, 1% IGEPAL CA-630 and 1% Na deoxycholate, three times), 1 × PXL buffer (1 × PBS with 0.1% SDS, 0.5% Na deoxycholate and 0.5% IGEPAL CA-630, two times), 5 × PXL buffer (5 × PBS with 0.1% SDS, 0.5% Na deoxycholate and 0.5% IGEPAL CA-630, two times) and PNK buffer (50 mM Tris-HCl, pH 7.4, 10 mM $MgCl_2$ and 0.5% IGEPAL CA-630, two times).

After dephosphorylation with calf intestinal alkaline phosphatase (Promega) at 37°C for 20 min and washes with buffer PNK-EGTA (50 mM Tris-HCl, pH 7.4, 20 mM EGTA and 0.5% IGEPAL CA-630, two times) and PNK (two times), a 3′ RNA adaptor with a phosphate on its 5′ end (RL3) was ligated to the 3′ end of RNAs using T4 RNA ligase 1 (NEB) at 16°C overnight. Next day, the resin was sequentially washed with buffer 1 × PXL (once), 5 × PXL (once) and PNK (three times). RNAs on the resin were treated with T4 PNK (NEB) at 37°C for 20 min and washed with buffer PNK (three times), Wash/Eq (once) and PK (100 mM Tris-HCl, pH 7.5, 50 mM NaCl and 10 mM EDTA, once). To release RNAs from the resin, proteins were digested with 4 mg/mL proteinase K (Roche) in PK buffer at 37°C for 20 min and further inactivated by 7 M urea dissolved in PK buffer at 37°C for 20 min. Free RNAs were extracted using phenol/chloroform and precipitated with ethanol/isopropanol at −20°C overnight. Next day, RNAs were pelleted, washed with 70% cold ethanol and resuspended in DEPC-treated H_2O. A 5′ RNA adaptor (RL5) with six degenerate nucleotides and a common 'G' on its 3′ end (RL5-NNNNNNG, RL5D-6N) was ligated to the purified RNAs using T4 RNA ligase 1 at 16°C for 5 hr. Then, the RNAs were treated with RQ1 DNase at 37°C for 20 min to remove residual DNAs and purified by phenol/chloroform extraction and ethanol/isopropanol precipitation.

Purified RNAs were reverse transcribed using the DP3 primer (final concentration: 0.5 μM) and Superscript III reverse transcriptase (Invitrogen). The resulting cDNAs were amplified with primers DP3 and DP5 (final concentrations: 0.5 μM) and Accuprime Pfx DNA polymerase (Invitrogen) to the optimal amplification point. The optimal amplification cycle (defined as the cycle before the PCR reaction reaching a plateau) was preliminarily determined by a diagnostic PCR visualized on gel or a real-time PCR with SYBR green (Invitrogen). PCR products of miRNAs (HEAP miRNA library, expected size: 65 bp) and targets (HEAP mRNA library, expected size range: 75~200 bp) were resolved on a 15% TBE-Urea polyacrylamide gel (Invitrogen) and extracted separately (Figure S1A). To construct library for high-throughput sequencing, DNA primers DP3-barcodeX ("X" stands for barcode index) and DSFP5 (final concentrations: 0.33 μM) containing Illumina adaptors, sequencing primer binding sites and Illumina TruSeq indexes for multiplexing were introduced to the HEAP miRNA and mRNA libraries by PCR. Sequencing libraries were run on a 6% TBE polyacrylamide gel (Invitrogen) and purified.

To prepare input control library, RNAs in the lysates saved before the Halolink resin pulldown were dephosphorylated with calf intestinal alkaline phosphatase and phosphorylated with T4 PNK. RNAs were then cleaned up using the MyONE Silane beads (ThermoFisher Scientific) as described in (Van Nostrand et al., 2016). Then, the 3′ RNA adaptor (RL3) was ligated to the purified RNAs at 16°C overnight. Next day, the ligated RNAs were purified using the MyONE Silane beads. Similar to the preparation of HEAP libraries, the RNAs were ligated to the 5′ RNA adaptor (RL5D-6N) at 16°C for 5 hr, treated with RQ1 DNase, purified, reverse transcribed to cDNAs and amplified by PCR using primers DP3 and DP5. PCR products ranging from 75 to 200 bp were resolved on a 15% TBE-Urea polyacrylamide gel and used for input library preparation (see HEAP library preparation).

See also Table S1 for oligos and adaptors used in library construction and sequencing.

HEAP mRNA and miRNA libraries, along with the matched input control libraries, were submitted to the Integrated Genomics Operation Core at Memorial Sloan Kettering Cancer Center for high-throughput sequencing. After quantification and quality control, libraries were pooled and run on a HiSeq 2500 in Rapid mode in a 100 bp or 125 bp single end run.

HEAP library preprocessing

Barcode removal

The 6 nt degenerate barcodes and the last nucleotide 'G' coming from the 5′ adaptor RL5D-6N (in total 7 nt) were removed from the beginning of reads and appended to the original read names, which later were used to distinguish duplicated reads produced at PCR amplification steps.

Adaptor removal and read quality control

The 3′ adaptor (5′-GTGTCAGTCACTTCCAGCGGGATCGGAAGAGCACACGTCTGAACTCCAGTCAC-3′) and bases with Phred quality score lower than 20 were trimmed from reads using cutadapt v1.15 or v1.17 (Martin, 2011). After trimming, reads shorter than 18 nt were discarded.

Alignment

Processed reads were aligned to the UCSC mm10 mouse genome using STAR v2.5.3a. Reads mapping to multiple loci or with more than 5 mismatches were discarded.

PCR duplicate removal

Reads mapped to the same locus with identical barcodes were considered PCR duplicates and therefore collapsed. This was achieved by storing aligned reads using chromosome names, strand information, positions of the first bases and the 7 nt barcodes as keywords. Representative reads of these unique events were written into a new BAM file, which was used for peak calling.

Peak calling

Peak calling was done using the unpublished package CLIPanalyze (https://bitbucket.org/leslielab/clipanalyze). The function findPeaks() was used to run multiple steps of analysis. First, the combined signal from uniquely aligned and PCR-duplicate-corrected reads from multiple replicates was convolved with the second derivative of a Gaussian filter. Zero-crossings of the convolved signal corresponded to edges of putative peaks. Second, read counting was run in putative peaks and in GENCODE-annotated gene exons with putative peaks subtracted, for both HEAP replicates and input control replicates. Library sizes for both HEAP and input control replicates were estimated using the read counts in exons outside of putative peaks. Third, using these library size estimates, differential read count analysis was performed between HEAP and input control read counts in putative peaks using DESeq2, and FDR-corrected *p-value*s (adjusted *p-value*s) were assigned to each peak. Peaks of size > 20 nt and read count log2FC > 0 in HEAP versus input control were selected for downstream analysis. Peaks were annotated as overlapping with 3′UTR, 5′UTR, exons, introns, intergenic regions, lncRNA, in that order, using GENCODE (vM17) annotation. Peaks overlapping with genes of types "lincRNA," "antisense," "processed_transcript," according to GENCODE, were annotated as lncRNA peaks.

For mESCs, peak calling was run with the following parameters in findPeaks(): count.threshold = 10, extend.slice = 10, bandwidth = 80, extend.peaks.in.genes = 150. The full set of peaks was generated by comparing three independent HEAP libraries against two input control libraries. To identify peaks in each individual replicate to assess reproducibility and in the cell number titration experiment, a single library was compared to the two input control libraries. For iCLIP, peak calling was run using a single iCLIP library (TT-FHAGO2) against a single control library (TT-AGO2) with the following parameters: count.threshold = 5, extend.slice = 50, bandwidth = 60, extend.peaks.in.genes = 150. For comparison with iCLIP, peak calling with the same parameters was run for each single HEAP library of comparable size against a single input control library (Figures 2F, S2D, and S2E).

For embryos, peak calling was run using HEAP in one wild-type (miR-17∼92-WT), two heterozygous (miR-17∼92-HET) and one homozygous knockout (miR-17∼92-KO) embryo against the four matching input control libraries using the following parameters: count.threshold = 5, extend.slice = 10, bandwidth = 80, extend.peaks.in.genes = 150. Then differential HEAP read count analysis was performed using DESeq2 v1.22.1 in miR-17∼92-KO against miR-17∼92-WT and miR-17∼92-HET libraries to determine miR-17∼92-dependent peaks.

For cortices of P13 mice, peak calling was run using the two HEAP libraries against the two matching input control libraries using the same parameters as for embryos. The same parameters were used for peak calling using CLEAR-CLIP in 12 replicates versus the input control libraries generated for HEAP. Differential HEAP read count analysis in HEAP versus input control was performed using DESeq2 v1.20.0.

For gliomas and cortices in adult mice, three HEAP libraries from each context were generated. Before peak calling, size factors Y of the six HEAP libraries were estimated using the byte sizes of corresponding BAM files. Then, BAM files for two glioma replicates and three cortex replicates were downsampled to similar sizes to the smallest glioma replicate using samtools v1.3.1 (Li et al., 2009) with scaling factors X = 1/Y. Peak calling was run using the six scaled HEAP libraries against the six matching input control libraries, using the same parameters as for embryos, to identify the set of putative peaks. As usual, only peaks of size > 20 nt and with log2FC > 0 in HEAP versus input control were used in downstream analysis. Furthermore, only peaks with average normalized read count > 10 in the three glioma replicates or in the three cortex replicates were selected. To identify significant peaks in gliomas, DESeq2 v1.20.0 for read counts in these selected peaks was run using the three glioma replicates against the three matching input control replicates.

To identify significant peaks in cortices, DESeq2 for read counts in these selected peaks was run using the three cortex replicates against the three matching input control replicates. Differential HEAP read counts analysis between gliomas and cortices was run in peaks with adjusted *p-value* < 0.05 (in HEAP versus input control).

For lung tumors, peak calling was run using two HEAP libraries generated from normal lungs, two HEAP libraries from KP tumors and three HEAP libraries from EA tumors against seven matching input control libraries, using the same parameters as for embryos. Peaks of size > 20 nt and with log2FC > 0 in HEAP versus input control were used in downstream analysis. Furthermore, only peaks with average normalized read count > 10 in the two normal lung replicates, in the two KP tumor replicates or in the three EA tumor replicates were selected. To identify significant peaks in each tumor type, DESeq2 v1.20.0 for read counts in these selected peaks was run using the tumor replicates against their matching input control replicates. To identify significant peaks in normal lungs, DESeq2 for read counts in the selected peaks was run using the two normal lung replicates against the two matching input control replicates. To compare peak intensities between KP and EA tumors, DESeq2 for read counts in peaks with adjusted *p-value* < 0.05 (in HEAP versus input control) was run using the three EA tumor replicates against the two KP tumor replicates. Since peak intensities in EA and KP highly correlate with each other, the five tumor replicates were grouped and used for downstream analysis. To compare peak signals between tumors and normal lungs, differential HEAP read count analysis was perform in peaks with adjusted *p-value* < 0.05 (in HEAP versus input control) between the five tumor replicates and the two normal lung replicates.

miRNA abundance estimates

Reads in the HEAP miRNA libraries were processed and filtered following the "Barcode removal" and the "Adaptor removal and read quality control" steps described in the "HEAP library preprocessing" section. Processed small RNA reads were aligned to a miRNA genome index built from 1,915 murine pre-miRNA sequences from miRbase version 21 (Kozomara et al., 2019) (ftp://mirbase.org/pub/mirbase/21/) using Bowtie v2.3.4 (Langmead and Salzberg, 2012), and these reads were considered true miRNA counts if they fell within ± 4 bps at each of the 5′ and 3′ end of the annotated mature miRNAs. PCR duplicates were removed as described in the "PCR duplicate removal" step in the "HEAP library preprocessing" section.

miRNA seed family data were downloaded from the TargetScan website at http://www.targetscan.org/mmu_71/mmu_71_data_download/miR_Family_Info.txt.zip. For miRNA family level analysis, read counts mapping to members of the same miRNA family were summed up.

mRNA abundance estimates

Input control libraries generated from gliomas and cortices were used to estimate mRNA abundance. Reads were counted at each gene locus using featureCounts v1.6.3 (Liao et al., 2014) with GENCODE (vM22) primary annotation. Differential gene expression analysis was performed using DEseq2 v1.20.0.

Motif discovery

Unbiased motif enrichment analysis

Frequencies of all k-nucleotide-long sequences (k-mers, k = 7) were calculated for sequences in selected peaks ($Freq_{selected}$) and background sequences ($Freq_{bg}$). The enrichment score for these 7-mers was calculated as log2FC = log2 (($Freq_{selected}$ + c) / ($Freq_{bg}$ + c)), where c was a small corrective value that depended on k, the number and size of peaks. K-mers with the highest log2FCs were then reported. This analysis was performed using functions calculateKmerBackground() and findKmerEnrich() in CLIPanalyze. For mESCs, peaks mapping to 3′UTR were selected and background sequences were defined as sequences of 3′UTRs outside of peaks. For brain and lung cancers, peaks differentially present in tumors and their tissues of origin (adjusted *p-value* < 0.1, absolute log2FC (tumor versus normal) > 0.5) were selected and compared against background sequences, defined as exon sequences of genes, in which peaks were identified.

Enrichment score calculation for miRNA seed matches

log2 enrichment score of miRNA seed matches in Figure 2B was calculated as log2 ($Freq_{3'UTR}$ / $Freq_{bg}$). $Freq_{3'UTR}$ was frequencies of 7-mer or 8-mer seed matches for miRNA seed families in 3′UTR peaks, while $Freq_{bg}$ was frequencies of these seed matches calculated in background sequences. Background sequences were defined as 3′UTR sequences outside of peaks.

HOMER de novo motif discovery

In mESC libraries, for the top 50 7-mers found by unbiased motif enrichment analysis, positions of their exact occurrences in 3′UTR peaks were found. Sequences of a 15-bp region around these occurrences were extracted and subjected to HOMER *de novo* motif discovery (Heinz et al., 2010), using 15-bp windows shifted 100 bp and 200 bp on both sides of the 7-mers (and excluding those overlapping with any of the 3′UTR peaks) as background sequences. Similarly, for glioma and cortex libraries, the top 50 7-mers found in each context were mapped to corresponding peak set and subjected to HOMER *de novo* motif discovery. For normal lung and lung tumor libraries, the top 70 7-mers from each context were used.

IDR analysis

IDR analysis was run using the python package at https://github.com/nboley/idr (Li et al., 2011). All putative peaks (size > 20 nt, log2FC > 0 for HEAP versus input control) were provided via parameter "–peak-list." Peaks called for individual replicates were scored using log2FC in HEAP versus input control and provided via parameter "–samples," separately for each pair of replicates. Peaks at IDR < 0.05 were considered reproducible.

HEAP coverage analysis

bigWig files for visualization of HEAP and input control libraries at 1 bp resolution were produced in the following way. First, deepTools bamCoverage v3.1.3 (Ramírez et al., 2016) with parameter "-bs 1–scaleFactor X" was used to produce bedGraph files. Here, size factors Y were estimated using DESeq2 applied to read counts in exons outside of peaks in all HEAP and input control libraries in a particular experimental model (mESCs, embryos, etc.) and then reciprocals X = 1 / Y were used as BAM coverage scaling factors. Only bedGraph signal in the standard chromosomes was selected. Then "bedtools sort" (bedtools v2.23.0 (Quinlan and Hall, 2010)) and bedGraphToBigWig v4 (Kent et al., 2010) were used to produce bigWig files. HEAP libraries were visualized using UCSC genome browser or IGV (Robinson et al., 2011).

To measure HEAP coverage of various peak sets in embryo libraries, peaks were first assigned to miRNA seed families by searching for the corresponding 7-mer and 8-mer seed matches in peak sequences. All miRNA seed families were ranked by abundance measured in miR-17∼92-WT embryo. Peaks containing seed matches for the top 31 miRNA families were chosen. Score matrices of 800 bp windows surrounding these peaks were generated from size-factor-corrected bigWigs using the ScoreMatrixList() function from the genomation package v1.14.0 (Akalin et al., 2015). Histograms of average score were produced using the function plotMeta(). Heatmaps were generated using the multiHeatMatrix() function and extreme values were removed before plotting using the winsorize parameter with values c(0,98).

QUANTIFICATION AND STATISTICAL ANALYSIS

Luciferase assays in Figures 1C and S3E were performed in triplicates and data were represented as mean ± SD. For Figures 2C and S5D, the fit with confidence intervals was produced using function 'geom_smoonth()' in R package ggplot using parameter 'method = "lm"' and all other parameters being default. For cumulative distribution function plots, p values were determined using two-sided Kolmogorov-Smirnov tests between indicated gene sets. For Figure 3B, p values were calculated using Chi-square tests. For Figure 3F, normalized counts determined by RNA-seq were plotted as mean ± SD and p values were determined using unpaired t tests. For Figure S5B, normalized mRNA counts were plotted as mean ± SD. All other statistical and quantitative analysis was described in detail in the previous sections.